Cell Reports
Medicine

Article

Restoring thalamocortical circuit dysfunction by correcting HCN channelopathy in *Shank3* mutant mice

Graphical abstract

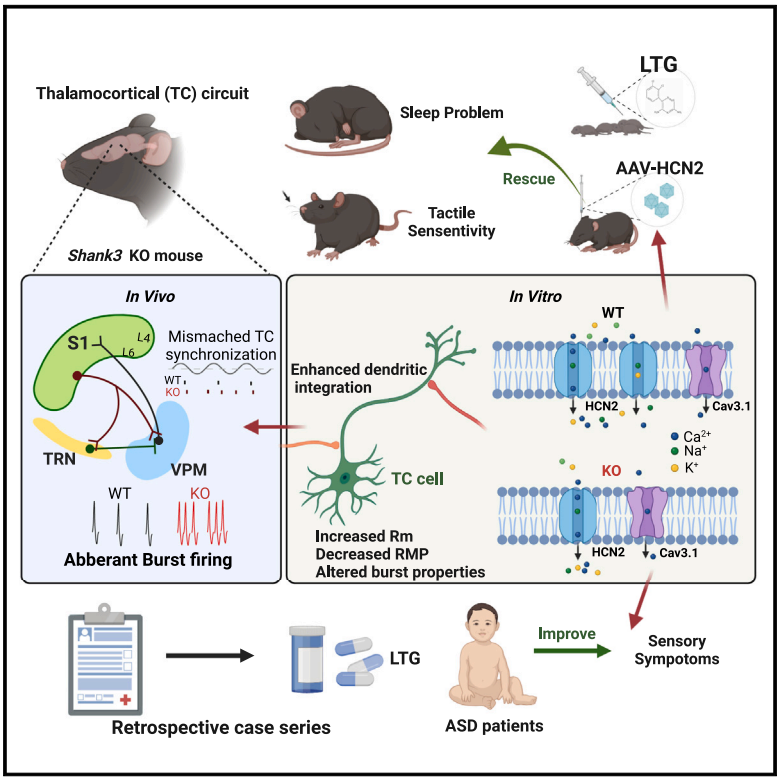

Highlights

- SHANK3 deficiency leads to increased excitability of thalamic relay neurons
- HCN2 channelopathy causally links sensory hypersensitivity and sleep fragmentation
- Early intervention targeting HCN2 channelopathy corrects ASD behavioral abnormalities
- Lamotrigine (LTG) treatment potentially benefits the sensory symptoms in ASD patients

Authors

Baolin Guo, Tiaotiao Liu, Soonwook Choi, ..., Michael M. Halassa, Shengxi Wu, Zhanyan Fu

Correspondence

shengxi@fmmu.edu.cn (S.W.), zfu@broadinstitute.org (Z.F.)

In brief

In a relevant mouse model of autism spectrum disorder (ASD), Guo et al. show increased excitability in thalamic neurons and disrupted phase-locking with cortical rhythms. Early intervention to restore HCN2 function with lamotrigine mitigates sensory hypersensitivity and sleep disturbances in this mouse model of ASD. This approach also holds promise for improving sensory behavior in ASD patients.

Guo et al., 2024, Cell Reports Medicine *5*, 101534
May 21, 2024
https://doi.org/10.1016/j.xcrm.2024.101534

CellPress

Cell Reports Medicine

CellPress
OPEN ACCESS

Article

Restoring thalamocortical circuit dysfunction by correcting HCN channelopathy in *Shank3* mutant mice

Baolin Guo,[1,2,7] Tiaotiao Liu,[4,7] Soonwook Choi,[2,3,7] Honghui Mao,[1,7] Wenting Wang,[1] Kaiwen Xi,[1] Carter Jones,[2] Nolan D. Hartley,[2,3] Dayun Feng,[1] Qian Chen,[3] Yingying Liu,[1] Ralf D. Wimmer,[3] Yuqiao Xie,[1] Ningxia Zhao,[5] Jianjun Ou,[6] Mario A. Arias-Garcia,[2] Diya Malhotra,[2] Yang Liu,[1] Sihak Lee,[2] Sammuel Pasqualoni,[2] Ryan J. Kast,[2,3] Morgan Fleishman,[2] Michael M. Halassa,[3] Shengxi Wu,[1,*] and Zhanyan Fu[2,3,8,*]

[1]Department of Neurobiology, School of Basic Medicine, Fourth Military Medical University, Xi'an 710032, China
[2]Stanley Center for Psychiatric Research, Broad Institute of MIT and Harvard, Cambridge, MA 02142, USA
[3]McGovern Institute for Brain Research, Department of Brain and Cognitive Sciences, MIT, Cambridge, MA 02139, USA
[4]School of Biomedical Engineering and Technology, Tianjin Medical University, Tianjin 300070, China
[5]Xi'an TCM Hospital of Encephalopathy, Shaanxi University of Chinese Medicine, Xi'an 710032, China
[6]Department of Psychiatry, The Second Xiangya Hospital of Central South University, National Clinical Research Center for Mental Disorders, Changsha 410011, China
[7]These authors contributed equally
[8]Lead contact
*Correspondence: shengxi@fmmu.edu.cn (S.W.), zfu@broadinstitute.org (Z.F.)
https://doi.org/10.1016/j.xcrm.2024.101534

SUMMARY

Thalamocortical (TC) circuits are essential for sensory information processing. Clinical and preclinical studies of autism spectrum disorders (ASDs) have highlighted abnormal thalamic development and TC circuit dysfunction. However, mechanistic understanding of how TC dysfunction contributes to behavioral abnormalities in ASDs is limited. Here, our study on a *Shank3* mouse model of ASD reveals TC neuron hyperexcitability with excessive burst firing and a temporal mismatch relationship with slow cortical rhythms during sleep. These TC electrophysiological alterations and the consequent sensory hypersensitivity and sleep fragmentation in *Shank3* mutant mice are causally linked to HCN2 channelopathy. Restoring HCN2 function early in postnatal development via a viral approach or lamotrigine (LTG) ameliorates sensory and sleep problems. A retrospective case series also supports beneficial effects of LTG treatment on sensory behavior in ASD patients. Our study identifies a clinically relevant circuit mechanism and proposes a targeted molecular intervention for ASD-related behavioral impairments.

INTRODUCTION

Given the complex nature and heterogeneity of autism spectrum disorder (ASD) etiology[1] researchers are faced with many challenges to decipher the pathophysiology and develop treatments, and ASD poses substantial mental and economic burdens on family and society.[2] To address the broad heterogeneity, researchers aim to identify convergent mechanisms on multiple levels, including molecular, cellular, and circuit levels, across diversified ASD risk genes. Along with others,[3,4] our studies [5–8] focus on synapse and circuit-level characterizations and exploring potential converging circuit-specific mechanisms underlying ASD-related behavioral impairments in animal models carrying genetically penetrant ASD risk genes, including *Shank3*. Besides the core symptom domains, patients with ASD often suffer from various comorbidities, such as sensory abnormalities, sleep disturbances, and seizures, making the development of therapeutic strategies even more difficult.

The thalamus is responsible for relaying sensory information to the cerebral cortex,[9] forming evolutionally conserved thalamocortical (TC) circuits that tightly regulate cortical excitability and functionality[10] and control multiple behaviors, including sensory processing,[11] sleep,[12] and cognition.[10] TC circuit dysfunction is implicated in abnormal tactile sensitivity, cognitive inflexibility, and sleep problems associated with ASDs and a subset of other neurodevelopmental disorders.[13–15] Clinical imaging and preclinical primate studies have suggested associations between structural and functional TC abnormalities in ASDs.[16–18] Furthermore, varied ASD risk genes are highly expressed in the thalamus (Allen Brain Atlas), including *Shank3*, *Mecp2*, and *Cntnap2*, reflecting a potential common vulnerability in TC circuits. However, the impact of ASD risk genes on TC circuit function and the consequent behavioral abnormalities remains largely unknown.

The prominent firing characteristics of TC relay cells are rhythmic and dynamic in different brain states,[19] conferred by the interplay between low-threshold T-type Ca^{2+} channels and

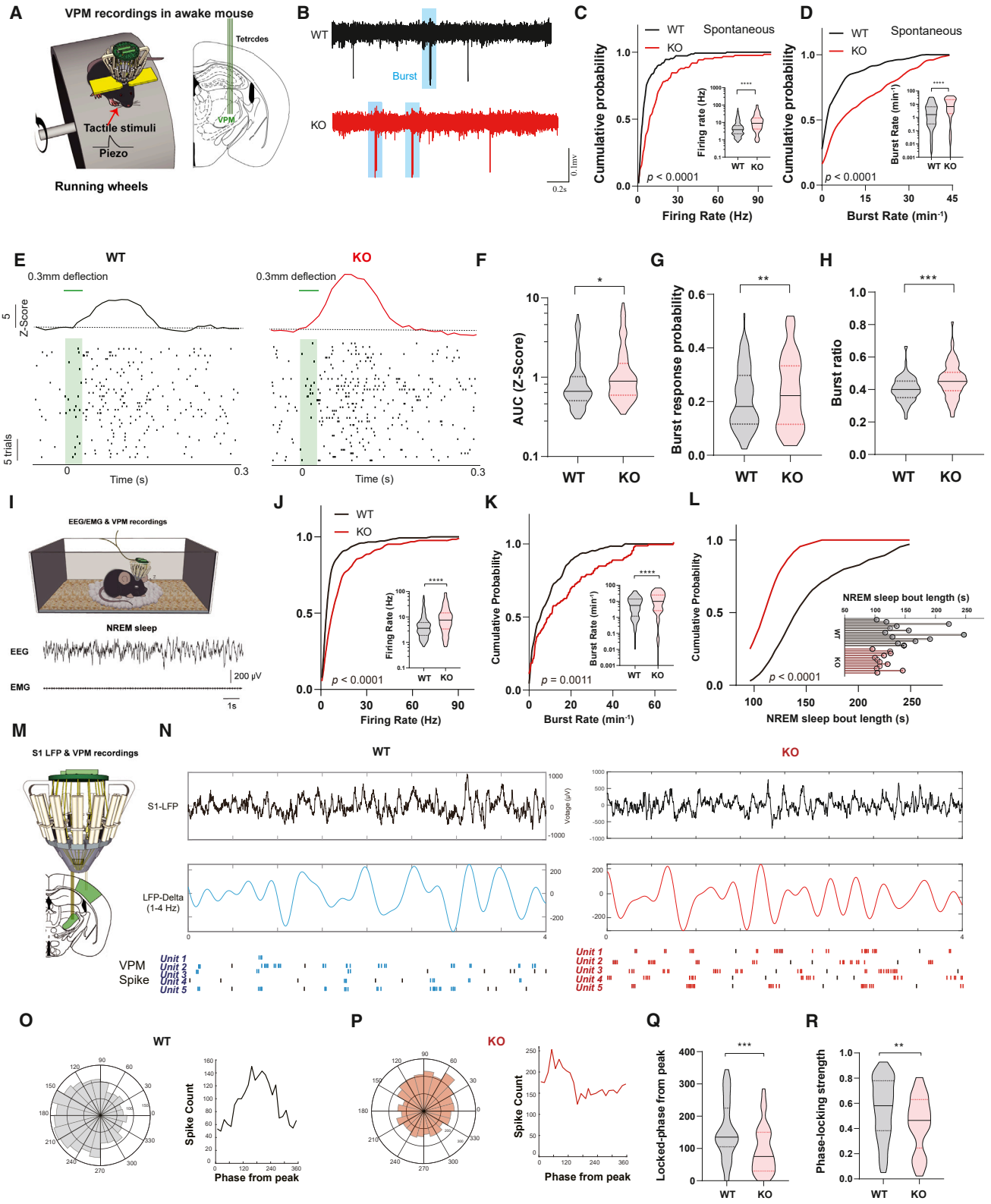

(legend on next page)

hyperpolarization-activated cyclic nucleotide-gated (HCN) channels.[20,21] Previous studies have revealed HCN channelopathy in an ASD mouse model and human induced pluripotent stem cells with *Shank3* mutations.[22,23] Yet, the link between HCN channelopathy, TC circuit dysfunction, and resulting behavioral abnormalities in *Shank3* mutants remains unexplored.

Here, we directly examined TC circuit physiological properties in awake and sleep states for both control wild-type (WT) and *Shank3* knockout (KO) mice. We found hyperexcitable TC cells with excessive burst firing and a temporal mismatched relationship with slow rhythmic cortical activity during sleep, attributed to HCN2 channel dysfunction in *Shank3* KO mice. Viral introduction of HCN2 or pharmacological enhancing HCN2 activity with lamotrigine (LTG) rescued sensory hypersensitivity and sleep fragmentation in *Shank3* KO mice. Additionally, the retrospective case series study showed that LTG treatment significantly benefitted sensory behavior in ASDs patients.

RESULTS

Altered firing dynamics of TC cells in awake *Shank3* KO mice

The well-studied somatosensory vibrissa pathway is known to involve the first-order somatosensory thalamic nucleus, the ventral posteromedial nucleus (VPM), which is specifically responsible for relaying sensory information from the whisker pad.[9] To directly test the excitability of TC cells in the VPM, we implanted multielectrode arrays in the VPM to monitor the neuronal firing activity in *Shank3* KO and control WT mice.

We first probed the VPM neuronal firing activity from awake mice, considering that the TC cell activity is dynamically modulated in a brain state-dependent manner.[24] The baseline neuronal activity was measured from head-fixed mice trained to stably walk on a rotating wheel[25] (Figure 1A). We found a significantly increased firing rate with excessive bursts of VPM TC cells in *Shank3* KO mice compared with WT mice (Figures 1B–1D). VPM cell bursting activity was originally believed to occur mostly during slow-wave sleep, when minimal sensory information is relayed by the thalamus. However, some studies have suggested that VPM burst firing may also play a role in small-amplitude whisker twitching in awake animals.[26,27] We thus further examined the whisker-evoked firing properties of TC cells. In line with our previous study,[6] we found that the relationship between thalamic neuronal firing and the intensity of tactile stimulation was not linear. Importantly, *Shank3* KO TC neurons exhibited not only markedly enhanced responsive trials featuring burst firing (Figures 1E–1G) but also a significantly increased number of bursts in these trials upon subtle 0.3-mm deflection (Figure 1H). For the maximal stimulus, 1.0-mm deflection, comparable neuronal responses were observed (Figures S1A–S1E).

Disrupted TC phase-locking relationship during sleep in *Shank3* KO mice

Both rodent and non-human primate *Shank3* mutant models exhibit sleep problems.[18,28] TC synchrony plays a crucial role in sustaining and pacing fundamental sleep rhythms.[29–31] We next investigated whether *Shank3* loss alters TC firing dynamics during sleep by simultaneously recording VPM TC activity along

Figure 1. *Shank3* deletion leads to neuronal hyperactivity and a mismatched TC locking relationship

(A) Schematic of head-fixed recordings in mice with multielectrode drive targeting the VPM to record spontaneous neuronal activity and tactile-evoked responses.

(B) Representative recording traces of VPM neurons in *Shank3* WT and KO. Blue shades mark the identified bursts.

(C) Cumulative probability plot of VPM spontaneous firing rates in *Shank3* WT and KO (left) and average firing rates of VPM neurons in *Shank3* WT and KO (right).

(D) Cumulative probability plot of VPM spontaneous burst rates in *Shank3* WT and KO (left) and average burst rates of VPM neurons in *Shank3* WT and KO (right).

(E) Example peri-stimulus time histograms (top) and rasters (bottom) showing tactile-evoked (20 ms, green bar) responses in *Shank3* WT and KO.

(F) Quantification of the area under curves (AUC) representing elevated neuronal responses of VPM neurons with 0.3-mm whisker deflection in *Shank3* KO mice.

(G) Probability of the burst occurrence in a trial, showing an increased proportion of trials featuring bursts in *Shank3* KO mice.

(H) Quantification of burst ratio, displaying increased burst numbers in all trials featuring bursts in *Shank3* KO mice.

(C–H) n = 147 neurons from 5 mice for WT; n = 123 neurons from 5 mice for KO.

(I) Schematic of VPM recordings coupling with EEG and EMG recordings with multielectrode drive *in vivo* (top) and Example traces of EEG and EMG during NREM natural sleep (bottom).

(J) Cumulative probability plot of VPM firing rates during NREM sleep in *Shank3* WT and KO (left) and average firing rates of VPM neurons in *Shank3* WT and KO (right). n = 147 neurons from 5 mice for WT; n = 123 neurons from 5 mice for KO.

(K) Cumulative probability plot of VPM burst rates during NREM sleep in *Shank3* WT and KO mice (left) and average burst rates of VPM neurons in *Shank3* WT and KO (right).

(L) Cumulative probability plot of NREM sleep bout length in *Shank3* WT and KO (left) and NREM sleep bout length of individual animals of *Shank3* WT and KO (right). n = 13 mice for WT; n = 12 mice for KO.

(M) Schematic of multielectrode drive targeting the VPM and somatosensory cortex (S1).

(N) Example traces of S1-LFP raw data (top), delta waves (1–4 Hz, center), and VPM spikes (bottom) during typical NREM sleep, showing the temporal alignment of VPM spikes to the preferred phase of the delta activity in WT (left) and KO mice (right). Blue and red dots mark the identified bursts.

(O) Spike distribution histogram for an example WT VPM neuron (left) and quantification of spike numbers with temporal alignment to different phases of LFP-delta of the S1 (right).

(P) Spike distribution histogram for an example KO VPM neuron (left) and quantification of spike numbers with temporal alignment to different phases of LFP-delta of the S1 (right).

(Q) Quantification of locked phase, showing a mismatched relationship between VPM spikes and S1-Delta LFP in *Shank3* KO mice.

(R) Quantification of locking strength in *Shank3* WT and KO mice.

For statistical comparisons, $^{**}p < 0.01$, $^{***}p < 0.001$, $^{****}p < 0.0001$. Two-tailed unpaired t test (C, D, F–H, J, K, Q, and R) and Kolmogorov-Smirnov test (C, D, J, and I). Detailed statistical information can be found in Data S1. Data are presented as median ± 95% CI.

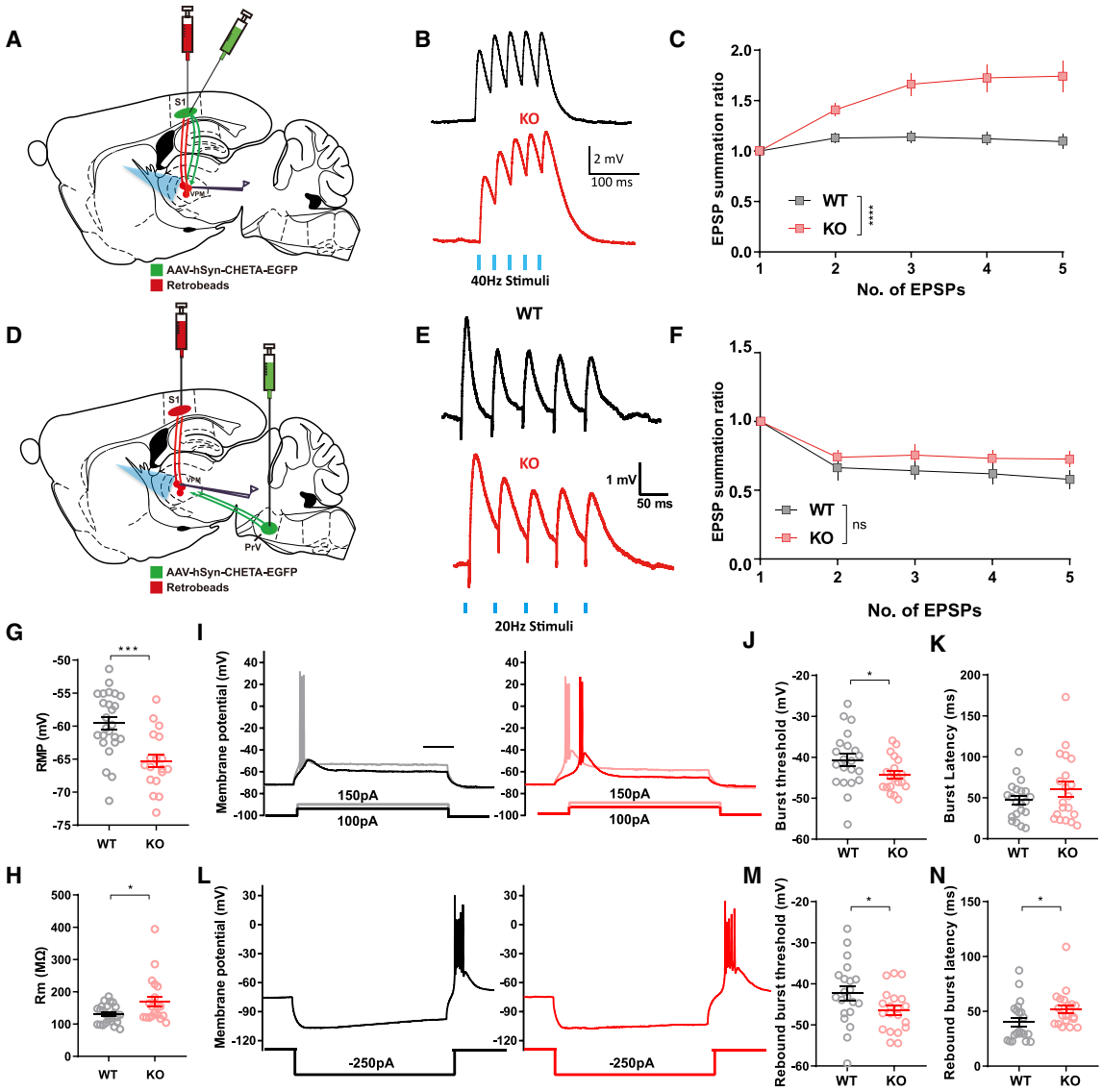

Figure 2. Enhanced dendritic integration and altered intrinsic properties of VPM neurons contribute to neuronal hyperactivity in *Shank3* KO mice

(A) Schematic of virus and Retrobead injections.

(B) Example traces of EPSPs with 40-Hz photoactivation.

(C) Quantification of EPSP summation ratio, showing that VPM cells show enhanced integration capability to cortical excitatory synaptic inputs. *n* = 11 neurons from 4 mice for WT; *n* = 15 neurons from 6 mice for KO.

(D) Schematic of virus and Retrobead injections.

(E) Example traces of EPSPs with 40-Hz photoactivation.

(F) Quantification of EPSP summation ratio, showing that VPM cells show intact integration capability to excitatory synaptic inputs from the brain stem. *n* = 7 neurons from 4 mice for WT; *n* = 9 neurons from 4 mice for KO.

(G) Summary of resting membrane potential (RMP) of VPM cells, showing that *Shank3* KO cells are more hyperpolarized compared with WT cells. *n* = 25 neurons from 7 mice for WT; *n* = 20 neurons from 5 mice for KO.

(H) Summary of membrane resistance (Rm) of VPM cells displaying a higher Rm of *Shank3* KO cells compared with WT cells. *n* = 25 neurons from 7 mice for WT; *n* = 20 neurons from 5 mice for KO.

(I) Representative traces of depolarization-induced bursts of VPM cells of *Shank3* WT (left) and KO (right) mice.

(J) Quantification analysis showing a decreased VPM burst threshold in *Shank3* KO cells.

(K) Quantification analysis denoting an unaltered burst latency in *Shank3* KO cells.

(L) Representative traces of rebound bursts of VPM cells of *Shank3* WT (left) and KO (right).

(M) Quantification analysis showing a reduced VPM rebound burst threshold in *Shank3* KO cells.

(legend continued on next page)

with electroencephalogram (EEG) and electromyogram (EMG) recordings, to distinguish between non-rapid eye movement (NREM) and rapid eye movement (REM) sleep (Figure 1I). *Shank3* KO TC cells exhibited significantly increased spike and burst rates during sleep (Figures 1J, 1K, and S2).

The spike timing of VPM TC cells has been reported to phase lock to slow oscillations in the primary somatosensory cortex (S1), and such a phase-locking relationship significantly contributes to NREM sleep regulation.[24] Indeed, the EEG/EMG recordings of *Shank3* KO mice showed fragmented NREM sleep with shorter sleep bout duration (Figure 1L). We measured the phase-locking relationship between TC cell firing and S1 local field potential (LFP) frequency band using custom multielectrode arrays (Figure 1M) and found an altered VPM-S1 phase-locking relationship in *Shank3* KO mice (Figures 1N–1P). At a population level, the averaged locked phase of TC cells in WT mice was preferentially at 135° after the LFP delta wave peak, whereas the averaged locked phase of KO cells was preferentially earlier (Figure 1Q). Also, we found weaker phase-locking strength in *Shank3* KO mice (Figure 1R).

VPM TC firing could also lock to the theta rhythm, one of the characteristic REM sleep waveforms.[24] We then tested the locking relationship between VPM firing and theta rhythm and observed an intact phase locking (Figures S3A–S3C) but with weaker locking strength (Figure S3D) in *Shank3* KO mice. Together, these results suggested that the hyperexcitability of TC cells with excessive burst firing in *Shank3* KO mice might lead to the altered TC locking relationship during distinct natural sleep stages.

Aberrant dendritic integration and intrinsic properties of TC cells in *Shank3* KO mice

The VPM TC cells receive ascending glutamatergic excitatory projections from the trigeminal complex and descending corticothalamic (CT) inputs from the S1[9] and inhibitory innervation exclusively from the thalamic reticular nucleus.[32–34] We injected Retrobeads, a non-toxic retrograde tracer, into the S1 and recorded the spontaneous miniature excitatory postsynaptic currents (mEPSCs) of the labeled TC cells. We found a significant decrease in the amplitude of mEPSCs in *Shank3* KO mice (Figure S4C) but no difference in the frequency (Figures S4A and S4B). We also recorded miniature inhibitory postsynaptic currents of TC cells and found no change in the frequency or the amplitude (Figures S4D–S4F). Consistent with our prior studies in other brain regions,[8,35,36] the synaptic transmission results suggested weaker excitatory synaptic drive, which would result in lower excitability, contrary to the observed hyperexcitability of TC cells in *Shank3* KO mice.

We, thus, proposed that other factors, such as alterations in dendritic integration and membrane intrinsic excitability, may counterbalance the reduced excitatory synaptic input. We injected an Adeno-associated virus (AAV) carrying a channelrhodopsin, CHETA, into the S1 and the trigeminal principal sensory nucleus (PrV), the two major excitatory input sources of the VPM. The paired pulse ratio (PPR) of TC cells was measured by stimulating the axonal terminals from descending S1 inputs or from ascending PrV inputs, and we found comparable PPRs (Figures S5A–S5F), suggesting intact presynaptic glutamatergic release properties in *Shank3* KO mice. We next measured dendritic synaptic integration properties of TC cells by delivering 40-Hz and 20-Hz optical stimulation, respectively, according to the differential kinetics between cortical and lemniscal synaptic properties.[37] The excitatory postsynaptic potential (EPSP) summation ratio of TC cells in *Shank3* KO mice was significantly larger than that of WT mice from cortical inputs but not from PrV inputs (Figures 2A–2F), suggesting greater synaptic integration of CT synapses in the *Shank3* KO mice.

We next measured the passive membrane properties of TC cells and found a more hyperpolarized resting membrane potential (RMP) (Figure 2G), a higher membrane resistance (Rm) (Figure 2H), and significantly reduced capacitance (Figure S6A) in *Shank3* KO mice. For active membrane properties, the TC cells are known to display two forms of burst firing when the RMP is hyperpolarized: depolarization-elicited bursts and hyperpolarization-induced rebound bursts.[38] Indeed, when the membrane potential of VPM TC cells was held at −75 mV, we observed the two forms of bursts by injecting either depolarizing or hyperpolarizing currents in both WT and *Shank3* KO mice (Figures 2I and 2L). The *Shank3* KO TC cells displayed a significantly lower burst threshold in both forms (Figures 2J and 2M). We also observed a significantly increased latency to rebound bursting (Figures 2K and 2N) in *Shank3* KO mice, suggesting a different burst onset. We further characterized the tonic firing properties at depolarized membrane potentials, as shown in Figure S6, with little difference in the various parameters of action potentials between genotypes.

Reduced HCN2 expression in VPM thalamic relay cells in *Shank3* KO mice

The TC burst firing is known to critically depend on the low-threshold T-type Ca^{2+} channel (Cav3.1) and HCN channels (HCN1, HCN2, and HCN4 in the VPM).[39] We measured the IT currents mediated by the Cav3.1 channels in the TC cells and found no significant difference in the current density between the *Shank3* KO and WT mice (Figure S7). We then examined hyperpolarization-activated current (Ih) mediated by HCN channels and found significantly lower Ih current density in *Shank3* KO TC cells of mice (Figures 3A–3C). To identify the isoforms of HCN channels responsible for the decreased Ih currents, we performed immunoblot analysis and found a significantly decreased expression level of HCN2 in *Shank3* KO mice but not HCN1 and HCN4 (Figures 3D and 3E). We further isolated the crude synaptoneurosomal fraction that contains dendrites and axonal processes[40] and found a significant reduction of HCN2 expression

(N) Quantification analysis denoting an increased rebound burst latency in *Shank3* KO cells.

(J, K, M, and N) $n = 21$ neurons from 7 mice for WT; $n = 20$ neurons from 5 mice for KO. For statistical comparisons, $^{*}p < 0.05$, $^{***}p < 0.001$, $^{****}p < 0.0001$. Friedman's M test (C), repeated-measurement ANOVA (F), two-tailed unpaired t test (G, J, and M); and Mann-Whitney U test (H, K, and N). Detailed statistical information can be found in Data S1. Data are presented as mean ± SEM.

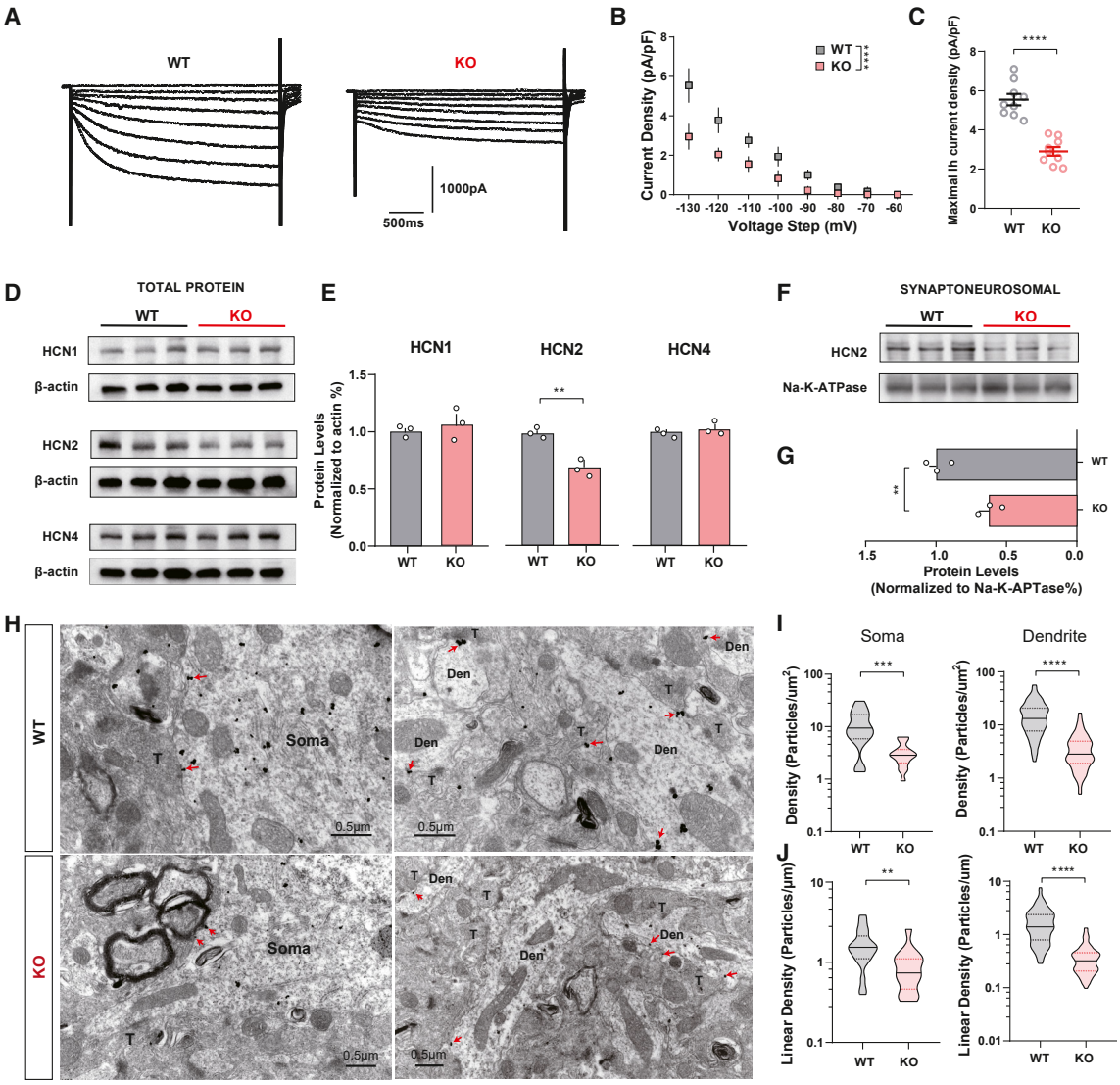

Figure 3. *Shank3* deletion impairs the function and expression of HCN2 channels in the VPM

(A) Representative traces of Ih currents in *Shank3* WT (left) and KO (right) cells.

(B) Summary of Ih current density with different voltage steps, showing decreased HCN mediated current density in *Shank3* KO cells.

(C) Quantification plot representing reduced maximal Ih current density in *Shank3* KO cells.

(B and C) $n = 9$ neurons from 3 mice for WT; $n = 9$ neurons from 3 mice for KO.

(D) Representative images of immunoblotting for HCN1, HCN2, and HCN4 of the VPM total protein in *Shank3* WT and KO.

(E) Quantification plot showing that the expression level of HCN2 is decreased in *Shank3* KO mice.

(F) Representative images of immunoblotting for HCN2 of the VPM synaptoneurosomal protein in *Shank3* WT and KO.

(G) Quantification plot showing that the expression level of HCN2 is reduced in *Shank3* KO mice.

(E and G) $n = 3$ mice for WT; $n = 3$ mice for KO.

(H) Representative immunogold micrographs showing the subcellular location of HCN2 (red arrows point to HCN2 in the membrane) in somatic (left) and dendritic regions (right) in *Shank3* WT (top) and KO (bottom). Scale bar: 0.5 μm.

(I) Density of HCN2-positive particles in somata (left) and dendrites (right).

(J) Linear density of HCN2-positive particles in the neuronal membranes in somata (left) and dendrites (right).

(I and J) $n = 20$ somata and 99 dendrites from 3 mice for WT; $n = 16$ somata and 95 dendrites from 3 mice for KO.

For statistical comparisons, $^{*}p < 0.05$, $^{***}p < 0.001$, $^{****}p < 0.0001$. Friedman's M test (B) and two-tailed unpaired t test (C, E, G, I, and J). Detailed statistical information can be found in Data S1. Data are presented as mean ± SEM (B, C, E, and G) and median ± 95% CI (I and J).

(Figures 3F and 3G), in line with the subcellular localization of HCN in a previous report.[41] Further HCN2 pre-embedding immunocytochemistry characterization under electron microscopy found that the HCN2 particles were distributed along the membrane of somata and dendrites as well as the Golgi complex in the cytoplasm (Figure 3H). Quantification revealed lower HCN2

CellPress
OPEN ACCESS

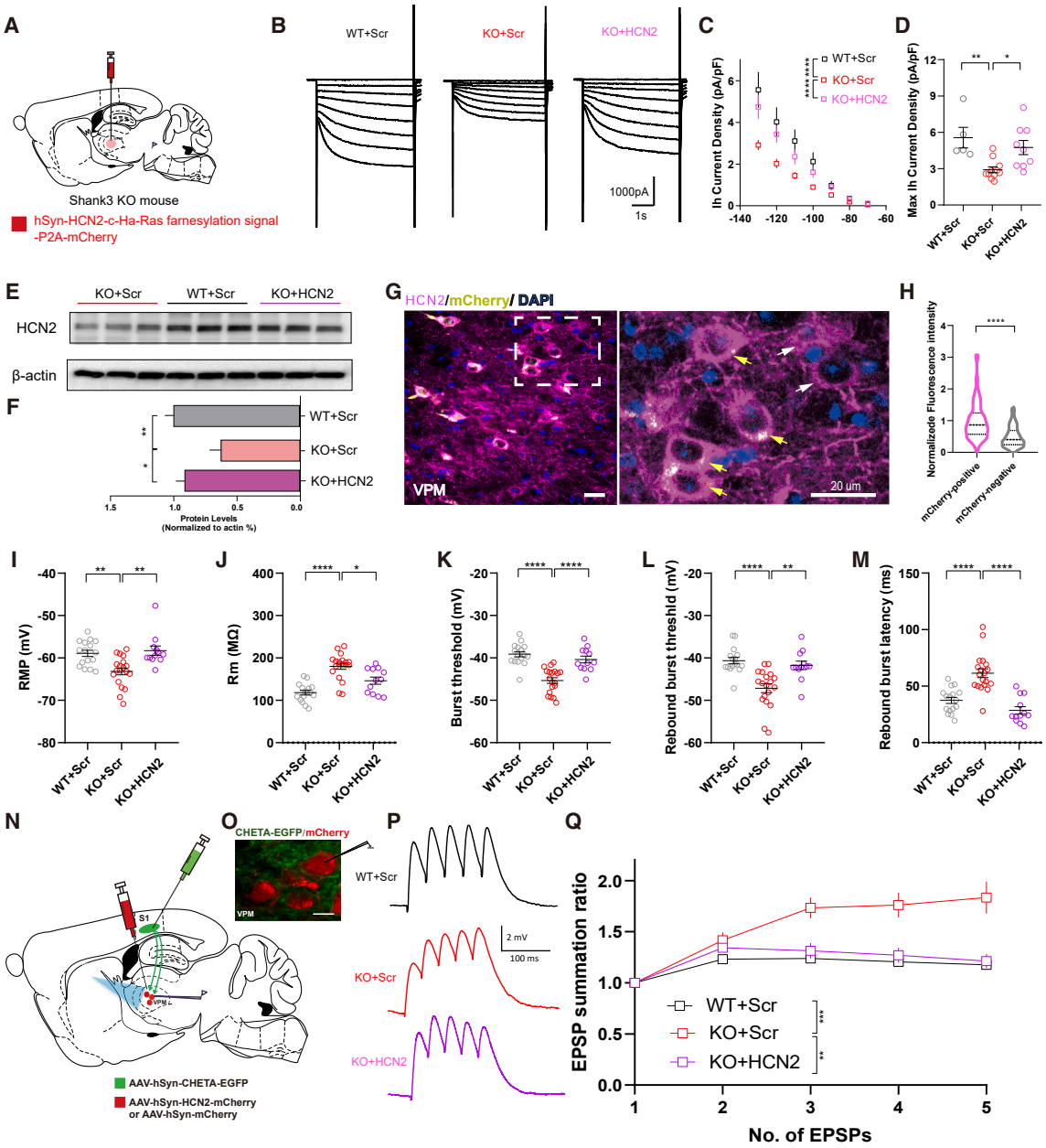

Figure 4. HCN2 overexpression in the VPM corrects electrophysiological alterations in *Shank3* KO mice

(A) Schematic of virus injection.

(B) Representative traces of Ih currents.

(C) Summary of Ih current density with different voltage steps, showing that the HCN2 overexpression (KO+HCN2) group displays increased Ih current density compared with the scramble (KO+Scr) group.

(D) Quantification plot representing increased maximal Ih current density in the KO+HCN2 overexpression (OE) group.

(C and D) n = 5 neurons from 3 mice for WT+Scr; n = 9 neurons from 3 mice for KO+HCN2; n = 11 from 3 mice for KO+Scr.

(E) Representative images of immunoblotting, showing the HCN2 expression level.

(F) Quantification of protein level, showing the effects of HCN2 OE in *Shank3* KO mice. n = 3 mice for WT+Scr; n = 3 mice for KO+HCN2; n = 3 mice for KO+Scr.

(G) Immunofluorescence images showing the HCN2 expression level in mCherry-positive (yellow arrows) and -negative cells (white arrows). Scale bar: 20 μm.

(H) Quantification of fluorescence intensity in mCherry-positive and -negative cells. n = 127 mCherry-positive neurons and n = 136 mCherry-negative neurons from 3 mice.

(I–M) Quantification of RMP (I), Rm (J), burst threshold (K), rebound burst threshold (L), and rebound burst latency (M), showing that HCN2 OE could rescue the intrinsic properties of VPM cells in *Shank3* KO mice. n = 16 neurons from 3 mice for WT+Scr; n = 12 neurons from 3 mice for KO+HCN2; n = 19 from 3 mice for KO+Scr.

(legend continued on next page)

particle density in somatic and dendritic areas of *Shank3* KO mice (Figure 3H), along with a significant decrease in membrane linear density compared to WT mice (Figure 3J).

HCN2 dysfunction contributes to VPM hyperactivity in *Shank3* KO mice

To investigate whether HCN channelopathy underlies TC cell electrophysiological alterations in *Shank3* KO mice, we introduced HCN2 channel expression in the VPM TC cells of P21 *Shank3* KO mice with an AAV vector carrying HCN2 tagged with membrane-targeted elements (Figure 4A). This resulted in significantly higher Ih current density in infected VPM TC cells in *Shank3* KO mice (Figures 4B–4D). Immunoblotting and histochemistry staining further confirmed the expression of the HCN2 channel in the cell membrane, and the protein level was elevated in the KO+HCN2 group (Figures 4E–4H). Whole-cell patch-clamp recordings showed that HCN2 re-expression in *Shank3* KO mice restored the hyperpolarized RMP and Rm (Figures 4I and 4J), corrected abnormal burst threshold and latency (Figures 4K–4M), and suppressed dendritic integration (Figures 4N–4Q).

Furthermore, using the selective HCN channel blocker ZD7288 on WT brain slices, we replicated *Shank3* KO-like firing dynamics, intrinsic membrane properties and synaptic integration (Figures S8A–S8O). In parallel, we applied ZD7288 in acute *Shank3* KO TC slices and found that ZD7288's effects were less pronounced in *Shank3* KO TC cells, except for rebound burst latency (Figures S8P–S8U). To further confirm whether the changes in rebound burst latency were HCN2 dependent in *Shank3* KO mice, we applied ZD7288 in acute *Shank3* KO TC slices overexpressing HCN2 or scrambled (Scr) control. TC cells overexpressing HCN2 exhibited more pronounced changes compared to those scrambled control cells (Figure S8V-X). Together, these results establish a direct causal link between HCN dysfunction and electrophysiological changes in *Shank3* KO mice.

The HCN2 channel as a potential therapeutic target

To explore the HCN channel as a potential therapeutic target for ASD-related behaviors, we selected two behavioral phenotypes in *Shank3* KO mice that critically depend on somatosensory TC circuits: tactile hypersensitivity[6] and sleep fragmentation.[28] We first used a viral strategy to overexpress the HCN2 channel or a scrambled control in P21 *Shank3* KO mice and assessed whisker-guided exploration and responses to whisker stimulation, respectively, following 1 month of viral HCN2 overexpression.[14,42] Consistent with prior studies,[6,43] we found that KO+Scr control mice spent significantly more time exploring the textured walls than WT+Scr mice (Figure S10A), suggesting that the *Shank3* KO mice displayed a better ability to distinguish the differential features of their environment. Moreover, the scores of whisker-elicited responses were higher in KO+Scr than WT+Scr mice. The KO+HCN2 group exhibited significantly lower scores of whisker-induced responses (Figures S10B and S10C) and improved durations of NREM sleep bouts (Figure S10D).

We then explored the possibility of developing pharmacological approaches to enhance the activity of HCN2 channels. Due to the lack of a specific HCN agonist, we leveraged a US Food and Drug Administration (FDA)-approved anticonvulsant LTG, which has been found to potentiate HCN channels.[44,45] First, we confirmed the LTP effects in acute TC brain slices. As shown in Figures 5A and 5B, we observed an increased Ih current density in *Shank3* KO TC cells upon LTG application in the recording solution. LTG also corrected the abnormalities of intrinsic properties (Figures 5C–5E and S11A) and dendritic integration in *Shank3* KO mice (Figures S11B and S11C). To rule out the possibility that LTG exerted the above effects through other ion channels, we bathed the slices with ZD7288 to completely block the HCN channel and subsequently applied LTG in the recording solution. The rescuing effects of LTG were abolished by ZD7288 pretreatment, supporting the HCN-dependent LTG rescue (Figures S11D–S11H). Next, we performed *in vivo* recordings with intraperitoneal injection of LTG in adult mice and found that LTG treatment reduced the firing rate and burst ratio in both awake and sleep states (Figures 5F–5I and 5L–5N). TC cells also exhibited a weaker response to 0.3-mm whisker deflection with less burst firing (Figures 5J and 5K). However, when we probed the locking relationship between the VPM firing and delta rhythm of S1 LFP during the NREM sleep stage, adult LTG treatment did not correct the mismatched phase locking in *Shank3* KO mice (Figure 5O), although the locking strength was improved (Figure 5P). During the REM sleep stage, LTG administration did not correct the impaired mismatch between VPM firing and theta rhythm in *Shank3* KO mice either (Figure S12). For the WT mice, we did not observe significant changes in all of these measurements, except for the firing rate after LTG treatment (Figure S13).

After administering a previously reported antidepressant dose of LTG (20 mg/kg) via intraperitoneal injection[46] (Figure 5Q), the KO+LTG mice spent significantly less time in textured zones than the KO+Vehicle (Veh) mice (Figure 5R). LTG treatment was able to normalize the response score to whisker stimulation in KO+LTG mice, comparable to the level of WT+Veh and WT+LTG mice (Figures 5S and 5T). However, LTG failed to improve sleep fragmentation in *Shank3* KO mice (Figure 5U), consistent with the persistent mismatch in phase-locking relationship between the VPM firing and S1 LFP (Figure 5O). Together, acute LTG administration in adult mice can mitigate tactile hypersensitivity but not sleep fragmentation of *Shank3* KO mice, suggesting that therapeutic reversal of ASD-related behavioral abnormalities might

(N) Schematic of virus injection and patch-clamp recordings.
(O) Representative images showing EGFP and mCherry expression in the VPM. Scale bar: 10 μm.
(P) Example traces of EPSPs with 40-Hz photoactivation.
(Q) Quantification of the EPSP summation ratio, showing that VPM cells show reduced integration capability to cortical excitatory synaptic inputs with HCN2 OE in *Shank3* KO mice. $n = 7$ neurons from 3 mice for WT+Scr; $n = 6$ neurons from 3 mice for KO+HCN2; $n = 10$ from 3 mice for KO+Scr.
For statistical comparisons, $^{*}p < 0.05$, $^{**}p < 0.01$, $^{***}p < 0.001$, $^{****}p < 0.0001$. Friedman's M test (C), one-way ANOVA (D, F, and I–M), two-tailed unpaired t test (H), and repeated-measurement ANOVA (Q). Detailed statistical information can be found in Data S1. Data are presented as mean ± SEM.

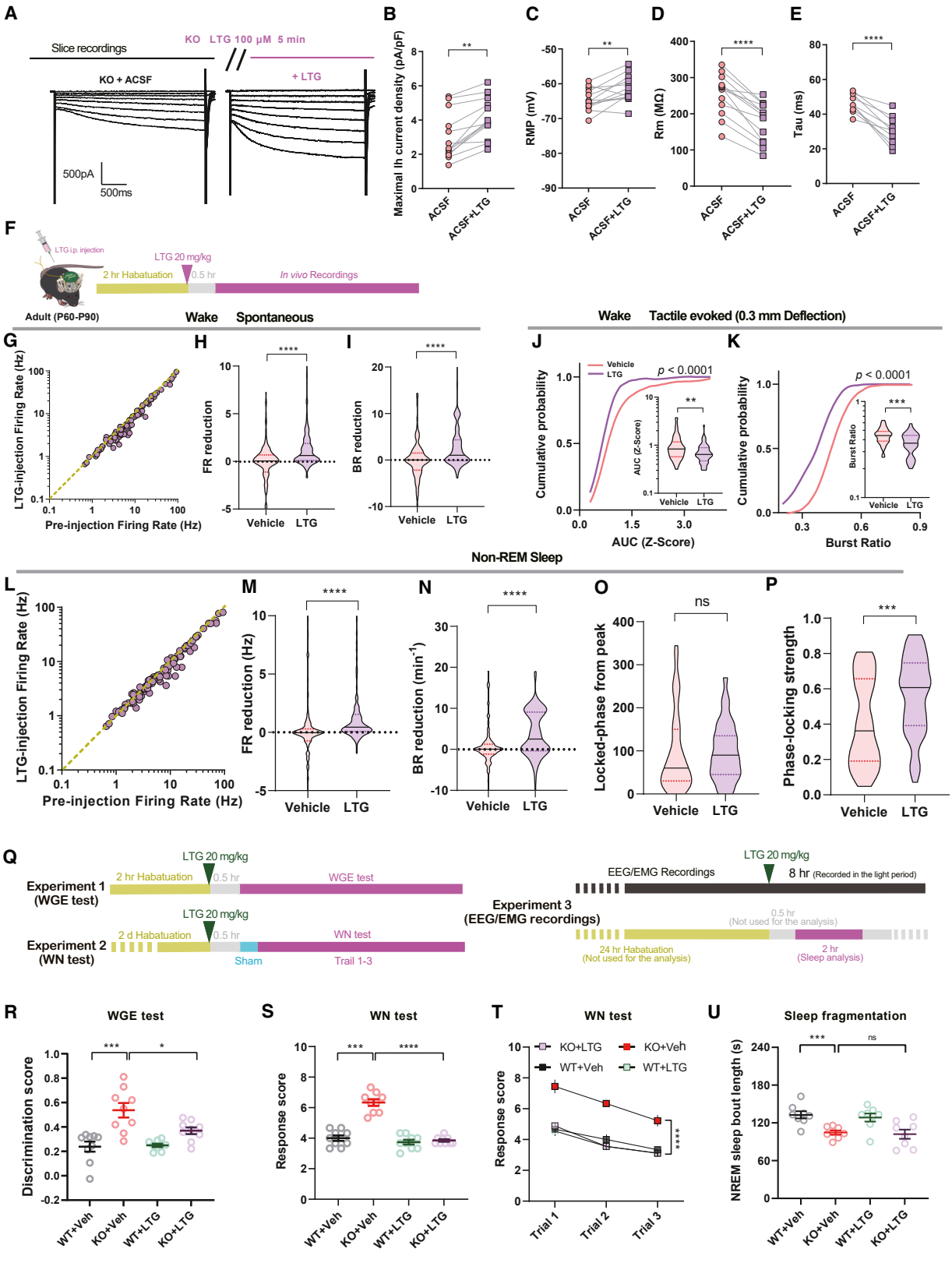

(legend on next page)

need chronic pharmacological treatment in adulthood or developmental interventions.

Developmental HCN activation provides long-lasting rescue

To explore the possibility of developmental interventions, we started examining whether HCN dysfunction in *Shank3* KO mice occurs earlier than the synaptic deficits during development. We recorded Ih and mEPSCs in the VPM TC cells at three postnatal time points (post-natal day 7 [P7], P14, and P21). We observed dynamic changes in synaptic development, with intact synaptic transmission at P7 but noticeable synaptic defects by P14, marked by a significant reduction in the frequency and peak amplitude of mEPSCs in *Shank3* KO mice (Figure S14). At P21, only the peak amplitude, but not frequency, of mEPSCs was significantly decreased. By contrast, *Shank3* deficiency caused a significant reduction in the Ih current density as early as P7, which lasted throughout the entire three postnatal developmental stages examined (Figure S15), suggesting that HCN channelopathy could be a potential pathophysiological mechanism independent of the later onset of synaptic defects.

We then administered a 5-day LTG treatment at three time points: P7, P14, and P21, aiming to restore HCN activity (Figure S16). The treatment from P7–P11 partially restored HCN activity in adult *Shank3* KO mice (Figure 6C; Figures S16A–S16C). By implanting multielectrode arrays into the animals treated with LTG or vehicle, we observed a reduction in overall firing rate (Figures 6D and 6H), burst firing (Figures 6E and 6I), and neuronal responses to whisker stimulation (Figures 6F and 6G). Importantly, the TC phase-locking relationship with the slow rhythmic S1 LFP in KO+LTG mice was fully corrected (Figures 6J–6L).

In line with the phase locking rescue, the KO+LTG mice exhibited comparable exploration time in the textured zones with the WT+Veh mice in the whisker-guided exploration test (Figure 6M) and significantly decreased response scores upon whisker stimulation, on par with the WT+Veh levels (Figures 6N and 6O). Furthermore, the 5-day LTG treatment markedly increased the duration of sleep bouts and corrected sleep fragmentation in *Shank3* KO mice (Figure 6P). These results demonstrated that early developmental restoration of HCN function could amend disrupted TC circuitry function, substantially mitigating both tactile hypersensitivity and sleep fragmentation.

To explore the effects of chronic LTG treatment on adult mice especially on sleep fragmentation, we administered 7-day LTG treatment in adult *Shank3* KO and WT mice. We monitored their sleep for a week post treatment and found no improvement in NREM sleep duration in LTG-treated *Shank3* KO mice (Figures S17A and S17B). This highlights the critical timing of LTG treatment, indicating that earlier administration might yield better therapeutic results.

Beneficial effects of LTG treatment on sensory abnormalities in ASD patients

Given LTG's potential to ameliorate behavioral abnormalities in the ASD mouse model, we investigated its effects in patients with ASDs by conducting a multicenter case series. Since LTG is an FDA-approved antiepileptic drug (AED) but not for ASD-associated behavioral abnormalities alone, all ASD patients selected in this study had concurrent epilepsy, a common comorbidity in approximately one-third of ASD cases.[47] According to the treatment received, patients were grouped into a positive control group receiving levetiracetam (LEV) to rule out the possibility that AED therapy per se might improve behaviors by controlling epilepsy, a negative control group treated without any AED therapy to rule out placebo effects, and an experimental group receiving LTG primarily (Figure 7A). We assessed behavioral improvements according to the Autism Behavior Checklist (ABC) and Childhood Autism Rating Scale (CARS) by calculating

Figure 5. Acute administration of LTG rescues sensory hypersensitivity without normalization of sleep fragmentation and TC phase locking

(A) Representative traces showing the effect of LTG on Ih currents.
(B) LTG could increase the maximal Ih current density in *Shank3* KO VPM cells.
(C–E) LTG rescues passive membrane properties in *Shank3* KO VPM cells.
(B–E) $n = 13$ neurons from 7 mice.
(F) Schematic and workflow of *in vivo* recording design with LTG acute injection.
(G–I) Effects of LTG on spontaneous firing rate and burst rate in awake *Shank3* KO mice. $n = 142$ neurons from 5 mice for Veh; $n = 110$ neurons from 5 mice for LTG.
(J) Fraction plot showing the LTG effects on whisker-induced neuronal responses (left). Quantification of AUC denotes that LTG could decrease the hyperreactivity of VPM cells in *Shank3* KO mice.
(K) Fraction plot showing the LTG effects on whisker-induced burst response (left). Quantification of AUC denotes that LTG could decrease the burst ratio of VPM cells in *Shank3* KO mice.
(L–N) Effects of LTG on spontaneous firing rate and burst rate in NREM sleep in *Shank3* KO mice. $n = 142$ neurons from 5 mice for Veh; $n = 110$ neurons from 5 mice for LTG.
(O) Quantification of locked phase, representing no significant difference between LTG and vehicle groups.
(P) Quantification of locking strength, denoting that LTG could increase the locking strength in *Shank3* KO mice.
(Q) Schematic of behavioral test designs.
(R) Quantification of the discrimination score for the textured zone, showing decreased exploration preference in the textured zone in *Shank3* KO mice after LTG acute administration.
(S) Quantification of response scores following whisker stimulation in *Shank3* KO mice after LTG acute administration.
(T) Average response scores assigned to WT and *Shank3* KO mice during trials.
(R–T) $n = 9$ mice for all groups.
(U) Summary of NREM sleep bout length, showing no difference following LTG acute injection in *Shank3* KO mice. $n = 8$ mice for all groups.
For statistical comparisons, $^{*}p < 0.05$, $^{***}p < 0.001$, $^{****}p < 0.0001$. Wilcoxon signed-rank test (B), two-tailed paired t test (C–E), two-tailed unpaired t test (H–K and M–P), Kolmogorov-Smirnov test (J and K), Kruskal-Wallis H test (R and S), Friedman's M test (T), and one-way ANOVA (U). Detailed statistical information can be found in Data S1. Data are presented as mean ± SEM (B–E and R–U) and median ± 95% CI (H–K and M–P).

CellPress
OPEN ACCESS

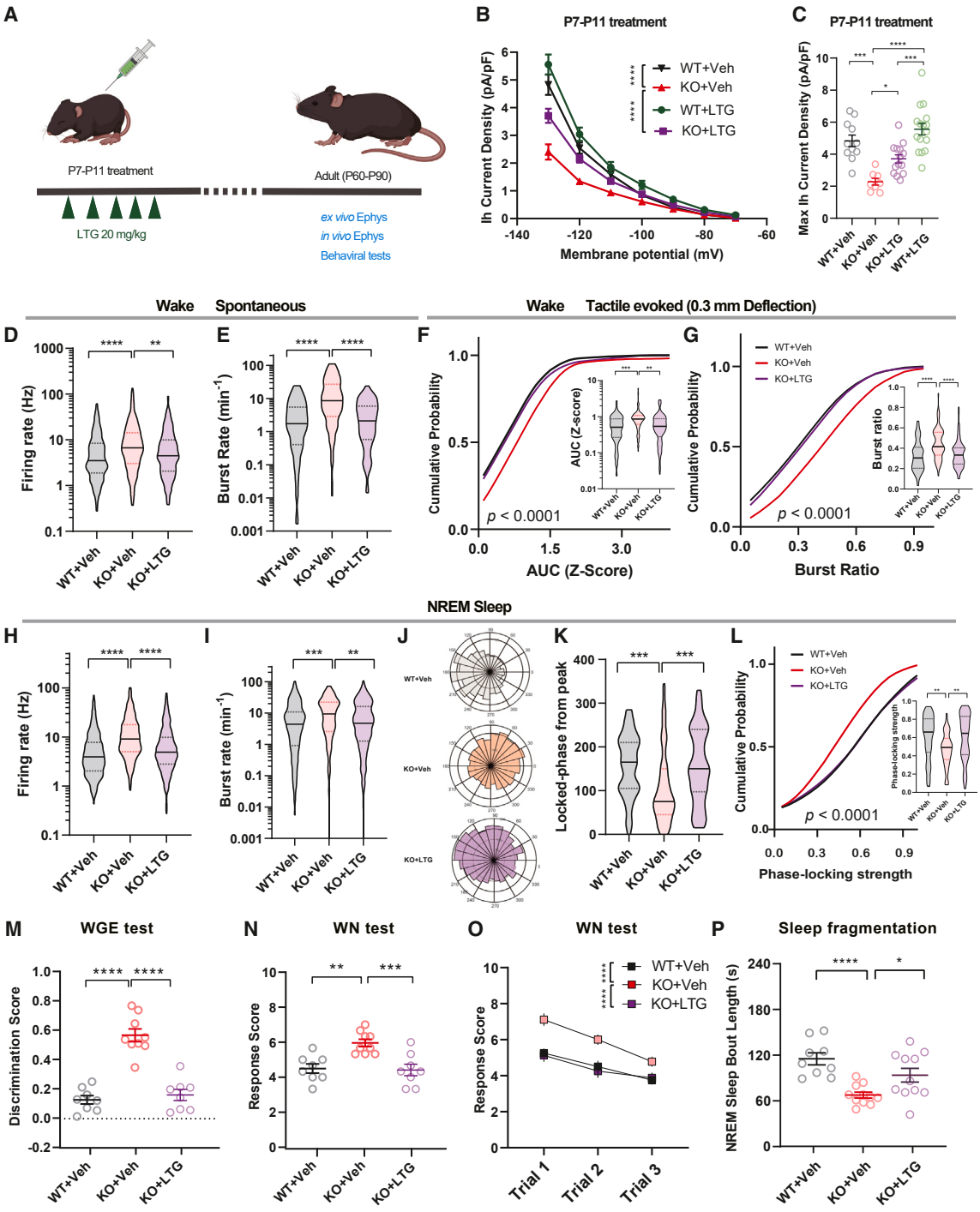

Figure 6. Early developmental treatment of LTG exerts long-lasting rescue effects in *Shank3* KO mice

(A) Schematic of experimental procedures.

(B) The Ih current density, showing the effects of LTG treatment during P7–P11 in *Shank3* WT and KO mice. $n = 11$ neurons from 3 mice for WT+Veh; $n = 8$ neurons from 3 mice for KO+Veh; $n = 16$ neurons from 3 mice for WT+LTG; $n = 14$ neurons from 3 mice for KO+LTG.

(C) Quantification of maximal Ih current density, showing that LTG treatment could boost Ih current in *Shank3* KO mice.

(D and E) Effects of a 5-day regimen of LTG on spontaneous firing rate and burst rate in awake *Shank3* KO mice. $n = 213$ neurons from 5 mice for WT+Veh; $n = 222$ neurons from 5 mice for KO+Veh; $n = 235$ neurons from 5 mice for KO+LTG.

(F) Fraction plot showing the effects of a 5-day regimen of LTG treatment on whisker-induced neuronal responses (left). Quantification of AUC denotes that LTG could decrease the hyper-reactivity of VPM cells in *Shank3* KO mice.

(legend continued on next page)

weighted mean differences (WMDs) and 95% confidence intervals (CIs).

We found that the LTG group showed substantial beneficial effects in the sensory section of ABC scores (WMD, 4.34; 95% CI, 3.32–5.36; $p < 0.01$) but not the LEV group (WMD, 0.42; 95% CI, −0.54–1.39; $p = 0.38$; Figure 7B). Intriguingly, when we examined the values of item 9 in CARS, which reflects tactile sensation, we found that LEV treatment lacked a net benefit (WMD, 0.11; 95% CI, 0.15–0.37; $p = 0.41$), whereas LTG treatment showed consistent beneficial effects (WMD, 0.11; 95% CI, 0.15–0.37; $p < 0.01$; Figure 7C). To account for patient variability in our study, we performed a multiple linear regression analysis, considering factors like gender, age, body weight, treatment season, observation duration, vital signs, baseline CARS and ABC scores, and medication treatment (Table S1). Our analysis identified medication treatment as the significant predictor for both ABC sensory score and CARS item 9 score, with gender also significantly affecting the CARS-item 9 score ($p = 0.019$).

For the total scores of ABC and CARS, LTG treatment showed consistent improvement, while LEV treatment displayed variable effects (Figures S18A and S18B). This suggests that LTG treatment exceeds the effects of sole anticonvulsant therapy in enhancing sensory behavior in ASD patients. Although promising, these preliminary findings from a small sampled retrospective case series study underscore the need for future large-sample and prospective studies to validate the efficacy and safety of LTG treatment for ASD-related abnormalities.

DISCUSSION

In the current study, we demonstrated for the first time a direct causal link between TC electrophysiological abnormalities, HCN2 channelopathy, and the consequent ASD-like behavioral phenotypes in a *Shank3* KO mouse model and further presented a rationale for the therapeutic potential through early intervention by correcting HCN channelopathy. Whether through gene therapy or pharmacological means, the early intervention can offer a promising approach to reduce the severity of ASD symptomatology by ameliorating tactile hypersensitivity and sleep fragmentation.

In the past decades, a growing body of evidence collected from ASD patients implicated the abnormal thalamic development and TC network.[17,48–52] TC circuits, critical hubs through which nearly all sensory information is routed, might represent a converging point of dysfunction across various neurodevelopmental disorders, as indicated by shared sensory and sleep phenotypes typical of these conditions. In line with previous studies,[23] *Shank3* deficiency led to an increased TC neuronal excitability with excessive burst firing. Additionally, our findings highlight a developmental progression of TC network dysfunction, aligning with previous studies showing early detection of TC alterations;[53] even 6-week-old children with high risk for ASDs demonstrate TC abnormalities,[16] much earlier than the emergence of clinical behavioral symptoms. This suggests TC dysfunction might serve as an early indicator for ASD diagnosis. In support of this, we observed Ih current density changes in TC cells from P7 in *Shank3* KO mice when synaptic transmission remains intact, suggesting that the channelopathy precedes synaptic defects of TC circuits.

Clinical observations have reported that children with ASDs often showed higher sensitivity to light touch and would feel uncomfortable with social touch. This somatosensory over-reactivity could be duplicated in the *Shank3* KO mice for both non-whisker-dependent[43,54] and whisker-dependent[6] tactile perceptions, accompanied by hyperactivity of the somatosensory cortex.[55] Although a recent study showed tactile hyposensitivity in the same strain of *Shank3* KO mice, the discrepancy may be caused by different observation parameters with our experiments.[56] For sleep fragmentation, our findings were consistent with previous reports in a *Shank3* KO primate model[18] and rodent model.[28] A recent study linked sensory sensitivities and sleep problems in ASDs patients to TC functional overconnectivity and elevated blood-oxygen-level-dependent signal amplitude.[13] Similarly, we found that correcting the TC hyperactivity in adult animals effectively rescued aberrant tactile sensitivities, in line with the finding where a $GABA_A$ receptor agonist significantly reduced tactile hypersensitivity.[43] However, unlike tactile hypersensitivity, ameliorating sleep abnormalities in *Shank3* KO mice required early developmental intervention, suggesting that diverse autistic behavioral abnormalities may arise at different developmental stages. Although SHANK3 plays an important role in directly regulating excitatory transmission as a synaptic scaffolding protein, rescuing sleep abnormalities in the *Shank3* KO model required early interventions targeting HCN2 channelopathy before synaptic dysfunction. This indicates a possibility that HCN channelopathy early in development could set the

(G) Fraction plot showing the effects of a 5-day regimen of LTG on whisker-induced burst response (left). Quantification of AUC denotes that LTG could decrease the burst ratio of VPM cells in *Shank3* KO mice.
(H and I) Effects of a 5-day regimen of LTG on spontaneous firing rate and burst rate in NREM sleep in *Shank3* KO mice. $n = 321$ neurons from 5 mice for WT+Veh; $n = 328$ neurons from 5 mice for KO+Veh; $n = 327$ neurons from 5 mice for KO+LTG.
(J and K) Spike distribution histograms (J) and quantification of the locked phase, representing that LTG corrects the locked phase in *Shank3* KO mice (K).
(L) Quantification of locking strength, denoting that LTG could increase the locking strength in *Shank3* KO mice.
(M) Quantification of the discrimination score for the textured zone, showing decreased exploration preference in the textured zone in *Shank3* KO mice receiving a 5-day regimen of LTG treatment.
(N) Quantification of response scores following whisker stimulation in *Shank3* KO mice receiving a 5-day regimen of LTG treatment.
(O) Average response scores during trials. $n = 8$ mice for WT+Veh; $n = 9$ mice for KO+Veh; $n = 8$ mice for KO+LTG.
(P) Summary of NREM sleep bout length, showing that a 5-day regimen of LTG treatment rescues sleep fragmentation in *Shank3* KO mice. $n = 9$ mice for WT+Veh; $n = 11$ mice for KO+Veh; $n = 11$ mice for KO+LTG.
For statistical comparisons, $^*p < 0.05$, $^{**}p < 0.01$, $^{***}p < 0.001$, $^{****}p < 0.0001$. Friedman's M test (B and O), one-way ANOVA (C–J and L–N), Kruskal-Wallis H test (P), and Jonckheere-Terpstra test (F, G, and K). Detailed statistical information can be found in Data S1. Data are presented as mean ± SEM (B, C, and M–P) and median ± 95% CI (D–L).

A

Retrospective case series (40 ASDs patients)

	No AED treatment (n = 15)	LEV treatment (n = 14)	LTG treatment (n = 11)
Age	5.19 ± 1.73	5.86 ± 2.46	8.61 ± 3.13
Weight	20.40 ± 5.97	23.79 ± 10.19	31.64 ± 13.94
ABC score (Baseline)	69.33 ± 11.48	70.29 ± 6.89	75.36 ± 14.36
CARS2-ST score (Baseline)	36.10 ± 2.76	35.29 ± 2.46	37.18 ± 2.69
Dose		47.14 ± 5.89	49.77 ± 8.95
Duration of observation regimen	103.00 ± 22.07	116.50 ± 31.28	111.00 ± 39.39

B

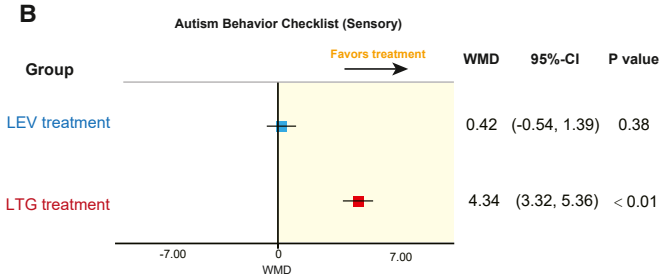

C

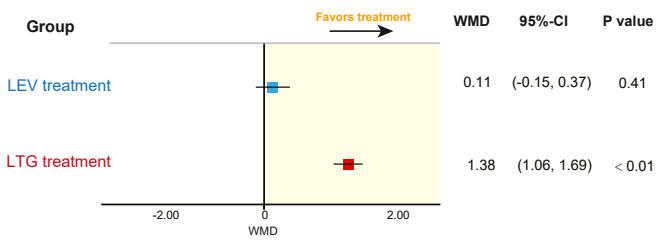

Figure 7. LTG treatment shows beneficial effects on hypersensitivity of ASDs patients

(A) Summary of patient characteristics.

(B) Forest plot showing the WMD value of the difference between the treatment and no-treatment group on ABC sensory score.

(C) Forest plot showing the WMD value of the difference between the treatment and no-treatment group on CARS (item 9) score.

Mann-Whitney U test. Data are presented as mean ± SD (A).

stage for a cascade of later neural alterations, including synaptic function and circuit connectivity. Once synaptic and circuit alterations have occurred, it may be challenging to reverse all behavioral issues in adulthood. This is supported by our prior studies showing that restoration of certain neural defects only rescued behavioral abnormalities partially or selectively in adulthood.[8,57] Thus, future studies aiming to understand the potential causal sequence by investigating the developmental interplay between HCN2 channels and SHANK3 are crucial.

Two recent studies revealed the relationship between the shankopathy and HCN channelopathy.[22,23] One study[22] reported the severe Ih current impairments in induced human neurons with *Shank3* mutation and identified the direct interaction between SHANK3 and three isoforms of HCN channels (including HCN2). Moreover, this study found that the HCN expression level could influence neuronal development. The other study[23] assessed the neuronal intrinsic properties and Ih current in two different *Shank3* mutations (PDZ domain mutation and ANK domain mutation), demonstrating that the PDZ domain was critical for the function of the HCN2 channel in the thalamus. Here, for the first time, we built the causal link between HCN2 dysfunction and *Shank3* deficiency-induced cellular, circuitry, and behavioral abnormalities. However, studies from autistic patients have revealed various mutations of the *Shank3* gene.[58] Considering the existence of distinct binding sites of SHANK3 to HCN channels,[22] future studies need to address whether interventions targeting Ih channelopathy can potentially be applied to all neurodevelopmental disease models with *Shank3* mutations or only to patients with mutations on HCN binding sites.

LTG, beyond the anti-epilepsy role, has also been approved for the maintenance treatment of bipolar disorder by the FDA and may also treat depression and mania.[59] It has shown potential in treating some symptoms in adult attention deficit hyperactivity disorder (ADHD)[60–62] and ASDs,[63,64] though its effectiveness is controversial. Some clinical studies reported that LTG could improve attention and social eye contact in autistic children,[64] while another randomized controlled trial reported no effect based on the checklists of diagnostic autistic behavioral criteria.[65] These mixed observations are potentially due to patient differences in genetics, prior treatments, and symptom diversity. Nevertheless, even in cases where HCN channels remain intact, targeting TC circuits still presents a promising approach benefitting a broader range of ASD patients with TC dysfunction. However, translating these findings to clinical settings requires caution due to developmental differences between rodents and humans. For example, the brains of rodents and humans evolve at significantly different rates, suggesting that the therapeutic window identified in mice in the current study might not directly apply to humans. A previous study indicates that the P7–P11 stage in mice approximates the third trimester in human gestation.[66] This highlights the need for comprehensive future research to carefully assess the potential for human application in clinical practice. Additionally, concerns have been raised about LTG use during pregnancy due to a potentially increased ASD and ADHD risk in offspring,[67] though this finding is considered controversial by a different study.[68] Also, all patients selected in our case series study had complications of epilepsy without clear genetic background information. Therefore, future research should rigorously assess LTG's therapeutic potential in humans, considering drug dosage and timing, especially in ASD patients without epilepsy and with diversified genetic backgrounds.

The pharmacology of LTG is complex; in addition to its effects on HCN channels, LTG inhibits various ion channels impacting neurotransmission, suggesting potential off-target effects. Importantly, we observed that LTG's efficacy was more pronounced during the sleep state, when TC cell membrane potentials were more hyperpolarized. HCN channels are known to be hyperpolarization activated and, therefore, are relatively more active in VPM TC cells during NREM sleep. This observation further supports the notion that LTG's effects on behavior primarily rely on the HCN channel. Additionally, addressing the appropriate intervention time window, drug dosage, and specific indications is crucial for clinical application. For the long-term effects of LTG developmental treatment, we found observable differences in the maximal Ih current density between the WT+LTG and KO+LTG groups, suggesting the possibility of partial rescue of HCN2 expression level in KO mice. However, the correction of TC circuit phase-locking and behavioral deficits in the *Shank3* KO mice suggests that the restoration of HCN function after P7–P11 LTG treatment could be contributed by other factors, such as the possibility of LTG treatment affecting regulatory mechanisms of HCN channel activity involving broad cellular signals other than solely expression level.[69] Also, evidence from biochemistry studies implied that HCN2 had its distinct cellular modulations different from other isoforms.[70] Thus, studying the cellular mechanisms of HCN activity in both animal and human stem cell models carrying cell-type-specific mutation will fuel the development of HCN isoform-targeted therapy in the future.

Our current findings from a small-scale retrospective clinical study should be approached with caution, noting biases such as patient age differences (LTG treatment group patients were generally older than other groups, likely due to clinical medication practices), side effect-induced self-selection (the potential for skin rash with LTG, along with the necessity for a titration approach to dosing, leading to some patients who are intolerant to these effects self-selecting out of this treatment group),[71] and potential socioeconomic skewing (our study required longitudinal data by selecting patients with extended hospital stays, necessary for multiple comprehensive assessments. This criterion may have inadvertently skewed our sample toward patients and families with higher socioeconomic status and educational levels). Additionally, one of the side effects of LEV is increased irritability in patients.[72] Using LEV as a comparator, given its irritability side effect, could affect the assessment of LTG's behavioral improvements. These preliminary clinical insights overall emphasize the experimental nature of the use of LTG in ASD patients, and there is a critical need for large-scale, prospective clinical trials before clinical adoption.

Limitations of the study

The study presents several limitations. First, the findings are based on the *Shank3* KO mouse model, and it remains unknown whether these results can be extrapolated to other ASD models with different genetic backgrounds. Second, while the study underscores the importance of early intervention by targeting HCN2 channelopathy, it also calls for further systematic investigation of therapeutic implications across different developmental stages. Third, the retrospective clinical study is limited by the representativeness of its patient cohort and insufficient data on treatment side effects. Therefore, it is critical to conduct future well-designed, prospective clinical trials to confirm the therapeutic benefits of LTG in ASD patients, especially those without epilepsy.

STAR★METHODS

Detailed methods are provided in the online version of this paper and include the following:

- KEY RESOURCES TABLE
- RESOURCE AVAILABILITY
  - Lead contact
  - Materials availability
  - Data and code availability
- EXPERIMENTAL MODEL AND STUDY PARTICIPANT DETAILS
  - Animal studies
  - Retrospective case studies
- METHOD DETAILS
  - Immunohistochemistry
  - Pre-embedding immunogold-silver cytochemistry
  - Viral vectors
  - Stereotaxic surgery
  - Western blot
  - Behavioral tests
  - Whisker guided exploration (WGE) test
  - Whisker Nuisance (WN) test
  - Sleep recordings and scoring
  - Slice electrophysiological recordings
  - *In vivo* electrophysiological recordings
  - Patients and data collection
- QUANTIFICATION AND STATISTICAL ANALYSIS

SUPPLEMENTAL INFORMATION

Supplemental information can be found online at https://doi.org/10.1016/j.xcrm.2024.101534.

ACKNOWLEDGMENTS

This work was supported by funding from the Stanley Center for Psychiatric Research at the Broad Institute (to Z.F.), the Natural Science Foundation of China (82221001 to S.W. and 82201699 to B.G.), and a project from the Ministry of Science and Technology of China (STI2030-2021ZD0201005 to S.W.). We thank Dr. Guoping Feng (MIT) for sharing the *Shank3* mutant mouse model, discussions, and expert input. We thank Dr. J. Kang, Dr. X. Huang (FMMU), Dr. Z. Zhou, and Dr. T. Zhou (MIT) for technical assistance; Ms. M. Garcia (MIT) for helping with MATLAB codes; Dr. M. Nakajima and Dr. L.I. Schmitt (RIKEN BSI) for guidance regarding *in vivo* recordings and data analysis; Dr. J. Voigts, Dr. D. Wang, and Dr. X. Gao (MIT) for valuable suggestions on behavioral paradigms; Dr. L. Yang (Broad Institute) for sharing the synaptoneurosomal preparation protocol; Dr. K. Chan and Dr. Q. Huang (Broad Institute) in Dr. Ben Deverman's lab for helpful discussion on viral strategies; Dr. Q. Wang (FMMU) for helpful discussion on clinical observation designs; Dr. S. Dai (Second Xiangya Hospital) for helping collect the clinical data; and HuSang Lee for assisting with sleep scoring in adult mice. The schematic and graphical abstract were created with BioRender with licenses.

AUTHOR CONTRIBUTIONS

B.G., S.W., and Z.F. conceived and designed the study. B.G., T.L., S.C., Q.C., and Y.L. (Yang Liu) performed *in vivo* recordings with the supervision of R.D.W., and M.M.H., B.G., and W.W. performed the slice recordings. S.C., K.X., M.M.H., C.J., Y.X., and M.F. performed behavioral tests. Y.L. (Yingying Liu) performed the electron microscopy experiments, and D.F. performed the western blot assay. Q.C., M.A.A.-G., D.M., S.P., R.J.K., and N.D.H.

provided technical assistance with electrophysiological recordings, behavior, surgery, and/or histology. T.L., S.C., S.L., C.J., and H.M. analyzed data. N.Z, J.O., and B.G. collected clinical data, and H.M. performed analysis. S.W. and Z.F. provided funding support and supervised the work. B.G. and Z.F. wrote the manuscript with input from all authors.

DECLARATION OF INTERESTS

The authors declare no competing interests.

Received: May 9, 2023
Revised: December 11, 2023
Accepted: April 4, 2024
Published: April 25, 2024

REFERENCES

1. Betancur, C. (2011). Etiological heterogeneity in autism spectrum disorders: more than 100 genetic and genomic disorders and still counting. Brain Res. *1380*, 42–77. https://doi.org/10.1016/j.brainres.2010.11.078.
2. Rogge, N., and Janssen, J. (2019). The Economic Costs of Autism Spectrum Disorder: A Literature Review. J. Autism Dev. Disord. *49*, 2873–2900. https://doi.org/10.1007/s10803-019-04014-z.
3. Choe, K.Y., Bethlehem, R.A.I., Safrin, M., Dong, H., Salman, E., Li, Y., Grinevich, V., Golshani, P., DeNardo, L.A., Peñagarikano, O., et al. (2022). Oxytocin normalizes altered circuit connectivity for social rescue of the Cntnap2 knockout mouse. Neuron *110*, 795–808.e6. https://doi.org/10.1016/j.neuron.2021.11.031.
4. Rothwell, P.E., Fuccillo, M.V., Maxeiner, S., Hayton, S.J., Gokce, O., Lim, B.K., Fowler, S.C., Malenka, R.C., and Südhof, T.C. (2014). Autism-associated neuroligin-3 mutations commonly impair striatal circuits to boost repetitive behaviors. Cell *158*, 198–212. https://doi.org/10.1016/j.cell.2014.04.045.
5. Roy, D.S., Zhang, Y., Aida, T., Choi, S., Chen, Q., Hou, Y., Lea, N.E., Skaggs, K.M., Quay, J.C., Liew, M., et al. (2021). Anterior thalamic dysfunction underlies cognitive deficits in a subset of neuropsychiatric disease models. Neuron *109*, 2590–2603.e13. https://doi.org/10.1016/j.neuron.2021.06.005.
6. Chen, Q., Deister, C.A., Gao, X., Guo, B., Lynn-Jones, T., Chen, N., Wells, M.F., Liu, R., Goard, M.J., Dimidschstein, J., et al. (2020). Dysfunction of cortical GABAergic neurons leads to sensory hyper-reactivity in a Shank3 mouse model of ASD. Nat. Neurosci. *23*, 520–532. https://doi.org/10.1038/s41593-020-0598-6.
7. Krol, A., Wimmer, R.D., Halassa, M.M., and Feng, G. (2018). Thalamic Reticular Dysfunction as a Circuit Endophenotype in Neurodevelopmental Disorders. Neuron *98*, 282–295. https://doi.org/10.1016/j.neuron.2018.03.021.
8. Guo, B., Chen, J., Chen, Q., Ren, K., Feng, D., Mao, H., Yao, H., Yang, J., Liu, H., Liu, Y., et al. (2019). Anterior cingulate cortex dysfunction underlies social deficits in Shank3 mutant mice. Nat. Neurosci. *22*, 1223–1234. https://doi.org/10.1038/s41593-019-0445-9.
9. O'Reilly, C., Iavarone, E., Yi, J., and Hill, S.L. (2021). Rodent somatosensory thalamocortical circuitry: Neurons, synapses, and connectivity. Neurosci. Biobehav. Rev. *126*, 213–235. https://doi.org/10.1016/j.neubiorev.2021.03.015.
10. Halassa, M.M., and Sherman, S.M. (2019). Thalamocortical Circuit Motifs: A General Framework. Neuron *103*, 762–770. https://doi.org/10.1016/j.neuron.2019.06.005.
11. Colonnese, M.T., and Phillips, M.A. (2018). Thalamocortical function in developing sensory circuits. Curr. Opin. Neurobiol. *52*, 72–79. https://doi.org/10.1016/j.conb.2018.04.019.
12. Halassa, M.M. (2011). Thalamocortical dynamics of sleep: roles of purinergic neuromodulation. Semin. Cell Dev. Biol. *22*, 245–251. https://doi.org/10.1016/j.semcdb.2011.02.008.
13. Linke, A.C., Chen, B., Olson, L., Ibarra, C., Fong, C., Reynolds, S., Apostol, M., Kinnear, M., Müller, R.A., and Fishman, I. (2023). Sleep Problems in Preschoolers With Autism Spectrum Disorder Are Associated With Sensory Sensitivities and Thalamocortical Overconnectivity. Biol. Psychiatry. Cogn. Neurosci. Neuroimaging *8*, 21–31. https://doi.org/10.1016/j.bpsc.2021.07.008.
14. Chelini, G., Zerbi, V., Cimino, L., Grigoli, A., Markicevic, M., Libera, F., Robbiati, S., Gadler, M., Bronzoni, S., Miorelli, S., et al. (2019). Aberrant Somatosensory Processing and Connectivity in Mice Lacking Engrailed-2. J. Neurosci. *39*, 1525–1538. https://doi.org/10.1523/JNEUROSCI.0612-18.2018.
15. Wells, M.F., Wimmer, R.D., Schmitt, L.I., Feng, G., and Halassa, M.M. (2016). Thalamic reticular impairment underlies attention deficit in Ptchd1(Y/-) mice. Nature *532*, 58–63. https://doi.org/10.1038/nature17427.
16. Nair, A., Jalal, R., Liu, J., Tsang, T., McDonald, N.M., Jackson, L., Ponting, C., Jeste, S.S., Bookheimer, S.Y., and Dapretto, M. (2021). Altered Thalamocortical Connectivity in 6-Week-Old Infants at High Familial Risk for Autism Spectrum Disorder. Cerebr. Cortex *31*, 4191–4205. https://doi.org/10.1093/cercor/bhab078.
17. Nair, A., Treiber, J.M., Shukla, D.K., Shih, P., and Müller, R.A. (2013). Impaired thalamocortical connectivity in autism spectrum disorder: a study of functional and anatomical connectivity. Brain *136*, 1942–1955. https://doi.org/10.1093/brain/awt079.
18. Zhou, Y., Sharma, J., Ke, Q., Landman, R., Yuan, J., Chen, H., Hayden, D.S., Fisher, J.W., 3rd, Jiang, M., Menegas, W., et al. (2019). Atypical behaviour and connectivity in SHANK3-mutant macaques. Nature *570*, 326–331. https://doi.org/10.1038/s41586-019-1278-0.
19. Llinás, R., Urbano, F.J., Leznik, E., Ramírez, R.R., and van Marle, H.J.F. (2005). Rhythmic and dysrhythmic thalamocortical dynamics: GABA systems and the edge effect. Trends Neurosci. *28*, 325–333. https://doi.org/10.1016/j.tins.2005.04.006.
20. McCormick, D.A., and Pape, H.C. (1990). Properties of a hyperpolarization-activated cation current and its role in rhythmic oscillation in thalamic relay neurones. J. Physiol. *431*, 291–318. https://doi.org/10.1113/jphysiol.1990.sp018331.
21. Anderson, M.P., Mochizuki, T., Xie, J., Fischler, W., Manger, J.P., Talley, E.M., Scammell, T.E., and Tonegawa, S. (2005). Thalamic Cav3.1 T-type Ca2+ channel plays a crucial role in stabilizing sleep. Proc. Natl. Acad. Sci. USA *102*, 1743–1748. https://doi.org/10.1073/pnas.0409644102.
22. Yi, F., Danko, T., Botelho, S.C., Patzke, C., Pak, C., Wernig, M., and Südhof, T.C. (2016). Autism-associated SHANK3 haploinsufficiency causes Ih channelopathy in human neurons. Science *352*, aaf2669. https://doi.org/10.1126/science.aaf2669.
23. Zhu, M., Idikuda, V.K., Wang, J., Wei, F., Kumar, V., Shah, N., Waite, C.B., Liu, Q., and Zhou, L. (2018). Shank3-deficient thalamocortical neurons show HCN channelopathy and alterations in intrinsic electrical properties. J. Physiol. *596*, 1259–1276. https://doi.org/10.1113/JP275147.
24. Urbain, N., Fourcaud-Trocmé, N., Laheux, S., Salin, P.A., and Gentet, L.J. (2019). Brain-State-Dependent Modulation of Neuronal Firing and Membrane Potential Dynamics in the Somatosensory Thalamus during Natural Sleep. Cell Rep. *26*, 1443–1457.e5. https://doi.org/10.1016/j.celrep.2019.01.038.
25. Reed, M.D., Yim, Y.S., Wimmer, R.D., Kim, H., Ryu, C., Welch, G.M., Andina, M., King, H.O., Waisman, A., Halassa, M.M., et al. (2020). IL-17a promotes sociability in mouse models of neurodevelopmental disorders. Nature *577*, 249–253. https://doi.org/10.1038/s41586-019-1843-6.
26. Fanselow, E.E., Sameshima, K., Baccala, L.A., and Nicolelis, M.A. (2001). Thalamic bursting in rats during different awake behavioral states. Proc. Natl. Acad. Sci. USA *98*, 15330–15335. https://doi.org/10.1073/pnas.261273898.
27. Swadlow, H.A., and Gusev, A.G. (2001). The impact of 'bursting' thalamic impulses at a neocortical synapse. Nat. Neurosci. *4*, 402–408. https://doi.org/10.1038/86054.

28. Ingiosi, A.M., Schoch, H., Wintler, T., Singletary, K.G., Righelli, D., Roser, L.G., Medina, E., Risso, D., Frank, M.G., and Peixoto, L. (2019). Shank3 modulates sleep and expression of circadian transcription factors. Elife *8*, e42819. https://doi.org/10.7554/eLife.42819.

29. Steriade, M. (2006). Grouping of brain rhythms in corticothalamic systems. Neuroscience *137*, 1087–1106. https://doi.org/10.1016/j.neuroscience.2005.10.029.

30. Gent, T.C., Bandarabadi, M., Herrera, C.G., and Adamantidis, A.R. (2018). Thalamic dual control of sleep and wakefulness. Nat. Neurosci. *21*, 974–984. https://doi.org/10.1038/s41593-018-0164-7.

31. Gent, T.C., Bassetti, C.L., and Adamantidis, A.R. (2018). Sleep-wake control and the thalamus. Curr. Opin. Neurobiol. *52*, 188–197. https://doi.org/10.1016/j.conb.2018.08.002.

32. Li, Y., Lopez-Huerta, V.G., Adiconis, X., Levandowski, K., Choi, S., Simmons, S.K., Arias-Garcia, M.A., Guo, B., Yao, A.Y., Blosser, T.R., et al. (2020). Distinct subnetworks of the thalamic reticular nucleus. Nature *583*, 819–824. https://doi.org/10.1038/s41586-020-2504-5.

33. Jones, E.G. (1975). Some aspects of the organization of the thalamic reticular complex. J. Comp. Neurol. *162*, 285–308. https://doi.org/10.1002/cne.901620302.

34. Paz, J.T., Bryant, A.S., Peng, K., Fenno, L., Yizhar, O., Frankel, W.N., Deisseroth, K., and Huguenard, J.R. (2011). A new mode of corticothalamic transmission revealed in the Gria4(-/-) model of absence epilepsy. Nat. Neurosci. *14*, 1167–1173. https://doi.org/10.1038/nn.2896.

35. Wang, W., Li, C., Chen, Q., van der Goes, M.S., Hawrot, J., Yao, A.Y., Gao, X., Lu, C., Zang, Y., Zhang, Q., et al. (2017). Striatopallidal dysfunction underlies repetitive behavior in Shank3-deficient model of autism. J. Clin. Invest. *127*, 1978–1990. https://doi.org/10.1172/JCI87997.

36. Peça, J., Feliciano, C., Ting, J.T., Wang, W., Wells, M.F., Venkatraman, T.N., Lascola, C.D., Fu, Z., and Feng, G. (2011). Shank3 mutant mice display autistic-like behaviours and striatal dysfunction. Nature *472*, 437–442. https://doi.org/10.1038/nature09965.

37. Mo, C., Petrof, I., Viaene, A.N., and Sherman, S.M. (2017). Synaptic properties of the lemniscal and paralemniscal pathways to the mouse somatosensory thalamus. Proc. Natl. Acad. Sci. USA *114*, E6212–E6221. https://doi.org/10.1073/pnas.1703222114.

38. Sherman, S.M. (2001). Tonic and burst firing: dual modes of thalamocortical relay. Trends Neurosci. *24*, 122–126. https://doi.org/10.1016/s0166-2236(00)01714-8.

39. Kanyshkova, T., Pawlowski, M., Meuth, P., Dubé, C., Bender, R.A., Brewster, A.L., Baumann, A., Baram, T.Z., Pape, H.C., and Budde, T. (2009). Postnatal expression pattern of HCN channel isoforms in thalamic neurons: relationship to maturation of thalamocortical oscillations. J. Neurosci. *29*, 8847–8857. https://doi.org/10.1523/JNEUROSCI.0689-09.2009.

40. Ghoshal, A., Uygun, D.S., Yang, L., McNally, J.M., Lopez-Huerta, V.G., Arias-Garcia, M.A., Baez-Nieto, D., Allen, A., Fitzgerald, M., Choi, S., et al. (2020). Effects of a patient-derived de novo coding alteration of CACNA1I in mice connect a schizophrenia risk gene with sleep spindle deficits. Transl. Psychiatry *10*, 29. https://doi.org/10.1038/s41398-020-0685-1.

41. Boyes, J., Bolam, J.P., Shigemoto, R., and Stanford, I.M. (2007). Functional presynaptic HCN channels in the rat globus pallidus. Eur. J. Neurosci. *25*, 2081–2092. https://doi.org/10.1111/j.1460-9568.2007.05463.x.

42. Balasco, L., Chelini, G., Bozzi, Y., and Provenzano, G. (2019). Whisker Nuisance Test: A Valuable Tool to Assess Tactile Hypersensitivity in Mice. Bio. Protoc. *9*, e3331. https://doi.org/10.21769/BioProtoc.3331.

43. Orefice, L.L., Mosko, J.R., Morency, D.T., Wells, M.F., Tasnim, A., Mozeika, S.M., Ye, M., Chirila, A.M., Emanuel, A.J., Rankin, G., et al. (2019). Targeting Peripheral Somatosensory Neurons to Improve Tactile-Related Phenotypes in ASD Models. Cell *178*, 867–886.e24. https://doi.org/10.1016/j.cell.2019.07.024.

44. Lehnhoff, J., Strauss, U., Wierschke, S., Grosser, S., Pollali, E., Schneider, U.C., Holtkamp, M., Dehnicke, C., and Deisz, R.A. (2019). The anticonvulsant lamotrigine enhances Ih in layer 2/3 neocortical pyramidal neurons of patients with pharmacoresistant epilepsy. Neuropharmacology *144*, 58–69. https://doi.org/10.1016/j.neuropharm.2018.10.004.

45. Omrani, A., van der Vaart, T., Mientjes, E., van Woerden, G.M., Hojjati, M.R., Li, K.W., Gutmann, D.H., Levelt, C.N., Smit, A.B., Silva, A.J., et al. (2015). HCN channels are a novel therapeutic target for cognitive dysfunction in Neurofibromatosis type 1. Mol. Psychiatr. *20*, 1311–1321. https://doi.org/10.1038/mp.2015.48.

46. Kaster, M.P., Raupp, I., Binfaré, R.W., Andreatini, R., and Rodrigues, A.L.S. (2007). Antidepressant-like effect of lamotrigine in the mouse forced swimming test: evidence for the involvement of the noradrenergic system. Eur. J. Pharmacol. *565*, 119–124. https://doi.org/10.1016/j.ejphar.2007.03.003.

47. Clarke, D.F., Roberts, W., Daraksan, M., Dupuis, A., McCabe, J., Wood, H., Snead, O.C., 3rd, and Weiss, S.K. (2005). The prevalence of autistic spectrum disorder in children surveyed in a tertiary care epilepsy clinic. Epilepsia *46*, 1970–1977. https://doi.org/10.1111/j.1528-1167.2005.00343.x.

48. Tamura, R., Kitamura, H., Endo, T., Hasegawa, N., and Someya, T. (2010). Reduced thalamic volume observed across different subgroups of autism spectrum disorders. Psychiatr. Res. *184*, 186–188. https://doi.org/10.1016/j.pscychresns.2010.07.001.

49. Haznedar, M.M., Buchsbaum, M.S., Hazlett, E.A., LiCalzi, E.M., Cartwright, C., and Hollander, E. (2006). Volumetric analysis and three-dimensional glucose metabolic mapping of the striatum and thalamus in patients with autism spectrum disorders. Am. J. Psychiatr. *163*, 1252–1263. https://doi.org/10.1176/appi.ajp.163.7.1252.

50. Ayub, R., Sun, K.L., Flores, R.E., Lam, V.T., Jo, B., Saggar, M., and Fung, L.K. (2021). Thalamocortical connectivity is associated with autism symptoms in high-functioning adults with autism and typically developing adults. Transl. Psychiatry *11*, 93. https://doi.org/10.1038/s41398-021-01221-0.

51. Mizuno, A., Villalobos, M.E., Davies, M.M., Dahl, B.C., and Müller, R.A. (2006). Partially enhanced thalamocortical functional connectivity in autism. Brain Res. *1104*, 160–174. https://doi.org/10.1016/j.brainres.2006.05.064.

52. Woodward, N.D., Giraldo-Chica, M., Rogers, B., and Cascio, C.J. (2017). Thalamocortical dysconnectivity in autism spectrum disorder: An analysis of the Autism Brain Imaging Data Exchange. Biol. Psychiatry. Cogn. Neurosci. Neuroimaging *2*, 76–84. https://doi.org/10.1016/j.bpsc.2016.09.002.

53. Toulmin, H., Beckmann, C.F., O'Muircheartaigh, J., Ball, G., Nongena, P., Makropoulos, A., Ederies, A., Counsell, S.J., Kennea, N., Arichi, T., et al. (2015). Specialization and integration of functional thalamocortical connectivity in the human infant. Proc. Natl. Acad. Sci. USA *112*, 6485–6490. https://doi.org/10.1073/pnas.1422638112.

54. Orefice, L.L., Zimmerman, A.L., Chirila, A.M., Sleboda, S.J., Head, J.P., and Ginty, D.D. (2016). Peripheral Mechanosensory Neuron Dysfunction Underlies Tactile and Behavioral Deficits in Mouse Models of ASDs. Cell *166*, 299–313. https://doi.org/10.1016/j.cell.2016.05.033.

55. Peixoto, R.T., Wang, W., Croney, D.M., Kozorovitskiy, Y., and Sabatini, B.L. (2016). Early hyperactivity and precocious maturation of corticostriatal circuits in Shank3B(-/-) mice. Nat. Neurosci. *19*, 716–724. https://doi.org/10.1038/nn.4260.

56. Balasco, L., Pagani, M., Pangrazzi, L., Chelini, G., Ciancone Chama, A.G., Shlosman, E., Mattioni, L., Galbusera, A., Iurilli, G., Provenzano, G., et al. (2022). Abnormal Whisker-Dependent Behaviors and Altered Cortico-Hippocampal Connectivity in Shank3b-/- Mice. Cerebr. Cortex *32*, 3042–3056. https://doi.org/10.1093/cercor/bhab399.

57. Mei, Y., Monteiro, P., Zhou, Y., Kim, J.A., Gao, X., Fu, Z., and Feng, G. (2016). Adult restoration of Shank3 expression rescues selective autistic-like phenotypes. Nature *530*, 481–484. https://doi.org/10.1038/nature16971.

58. Boccuto, L., Lauri, M., Sarasua, S.M., Skinner, C.D., Buccella, D., Dwivedi, A., Orteschi, D., Collins, J.S., Zollino, M., Visconti, P., et al. (2013). Prevalence of SHANK3 variants in patients with different subtypes of autism spectrum disorders. Eur. J. Hum. Genet. *21*, 310–316. https://doi.org/10.1038/ejhg.2012.175.

59. Besag, F.M.C., Vasey, M.J., Sharma, A.N., and Lam, I.C.H. (2021). Efficacy and safety of lamotrigine in the treatment of bipolar disorder across the lifespan: a systematic review. Ther. Adv. Psychopharmacol. *11*, 20451253211045870. https://doi.org/10.1177/20451253211045870.

60. Sablaban, I.M., and Sivananthan, M. (2022). Attention-Deficit Hyperactivity Disorder-Associated Impulsive Aggression Treated With Lamotrigine. Am. J. Therapeut. *29*, e747–e748. https://doi.org/10.1097/MJT.0000000000001219.

61. Han, S.A., Yang, E.J., Song, M.K., and Kim, S.J. (2017). Effects of lamotrigine on attention-deficit hyperactivity disorder in pediatric epilepsy patients. Korean J. Pediatr. *60*, 189–195. https://doi.org/10.3345/kjp.2017.60.6.189.

62. Öncü, B., Er, O., Çolak, B., and Nutt, D.J. (2014). Lamotrigine for attention deficit-hyperactivity disorder comorbid with mood disorders: a case series. J. Psychopharmacol. *28*, 282–283. https://doi.org/10.1177/0269881113493365.

63. Kumandas, S., Caksen, H., Ciftçi, A., Oztürk, M., and Per, H. (2001). Lamotrigine in two cases of Rett syndrome. Brain Dev. *23*, 240–242. https://doi.org/10.1016/s0387-7604(01)00191-7.

64. Uvebrant, P., and Bauzienè, R. (1994). Intractable epilepsy in children. The efficacy of lamotrigine treatment, including non-seizure-related benefits. Neuropediatrics *25*, 284–289. https://doi.org/10.1055/s-2008-1073041.

65. Belsito, K.M., Law, P.A., Kirk, K.S., Landa, R.J., and Zimmerman, A.W. (2001). Lamotrigine therapy for autistic disorder: a randomized, double-blind, placebo-controlled trial. J. Autism Dev. Disord. *31*, 175–181. https://doi.org/10.1023/a:1010799115457.

66. Workman, A.D., Charvet, C.J., Clancy, B., Darlington, R.B., and Finlay, B.L. (2013). Modeling transformations of neurodevelopmental sequences across mammalian species. J. Neurosci. *33*, 7368–7383. https://doi.org/10.1523/JNEUROSCI.5746-12.2013.

67. Yeh, T.C., Bai, Y.M., Hsu, J.W., Huang, K.L., Tsai, S.J., Chu, H.T., Liang, C.S., and Chen, M.H. (2021). Bipolar women's antepartum psychotropic exposure and offspring risk of attention-deficit/hyperactivity disorder and autism spectrum disorder. J. Affect. Disord. *295*, 1407–1414. https://doi.org/10.1016/j.jad.2021.09.016.

68. Wiggs, K.K., Rickert, M.E., Sujan, A.C., Quinn, P.D., Larsson, H., Lichtenstein, P., Oberg, A.S., and D'Onofrio, B.M. (2020). Antiseizure medication use during pregnancy and risk of ASD and ADHD in children. Neurology *95*, e3232–e3240. https://doi.org/10.1212/WNL.0000000000010993.

69. He, C., Chen, F., Li, B., and Hu, Z. (2014). Neurophysiology of HCN channels: from cellular functions to multiple regulations. Prog. Neurobiol. *112*, 1–23. https://doi.org/10.1016/j.pneurobio.2013.10.001.

70. Kusch, J., Biskup, C., Thon, S., Schulz, E., Nache, V., Zimmer, T., Schwede, F., and Benndorf, K. (2010). Interdependence of receptor activation and ligand binding in HCN2 pacemaker channels. Neuron *67*, 75–85. https://doi.org/10.1016/j.neuron.2010.05.022.

71. Egunsola, O., Choonara, I., and Sammons, H.M. (2015). Safety of lamotrigine in paediatrics: a systematic review. BMJ Open *5*, e007711. https://doi.org/10.1136/bmjopen-2015-007711.

72. Zhang, J.F., Piryani, R., Swayampakula, A.K., and Farooq, O. (2022). Levetiracetam-induced aggression and acute behavioral changes: A case report and literature review. Clin. Case Rep. *10*, e05586. https://doi.org/10.1002/ccr3.5586.

73. Kovács, K., Sík, A., Ricketts, C., and Timofeev, I. (2010). Subcellular distribution of low-voltage activated T-type Ca2+ channel subunits (Ca(v)3.1 and Ca(v)3.3) in reticular thalamic neurons of the cat. J. Neurosci. Res. *88*, 448–460. https://doi.org/10.1002/jnr.22200.

74. Carr, D.B., and Surmeier, D.J. (2007). M1 muscarinic receptor modulation of Kir2 channels enhances temporal summation of excitatory synaptic potentials in prefrontal cortex pyramidal neurons. J. Neurophysiol. *97*, 3432–3438. https://doi.org/10.1152/jn.00828.2006.

75. Whitmire, C.J., Waiblinger, C., Schwarz, C., and Stanley, G.B. (2016). Information Coding through Adaptive Gating of Synchronized Thalamic Bursting. Cell Rep. *14*, 795–807. https://doi.org/10.1016/j.celrep.2015.12.068.

STAR★METHODS

KEY RESOURCES TABLE

REAGENT or RESOURCE	SOURCE	IDENTIFIER
Antibodies		
Rabbit anti HCN1	Alomone labs	Cat. # APC-056; RRID: AB_2039900
Rabbit anti HCN2	Alomone labs	Cat. # APC-030; RRID: AB_2313726
Rabbit anti HCN4	Alomone labs	Cat. # APC-052; RRID: AB_2039906
Mouse anti β-actin	Cell Signaling Technology	Cat. # 3700; RRID: AB_2242334
Rabbit anti Na-K-ATPase	Cell Signaling Technology	Cat. # 3010; RRID: AB_2060983
Goat anti Rabbit IgG, Alexa Fluor 594	Thermo Fisher Scientific	Cat. # A-11012; RRID: AB_2534079
Nanogold IgG goat anti rabbit IgG (H + L)	Nanoprobes	Cat. # 2003; RRID: AB_2687591
Bacterial and virus strains		
AAV1-hSyn-CHETA-eYFP	Addgene	Cat. # 100049-AAV1; RRID:Addgene_100049
AAV1-hSyn-HCN2-c-Ha-Ras farnesylation signal-P2A-mcherry	OBiO Technology	N/A
AAV1-hSyn-c-Ha-Ras farnesylation signal-P2A-mcherry	OBiO Technology	N/A
Chemicals, peptides, and recombinant proteins		
Lamotrigine	Sigma Aldrich	Cat. #L3791
Critical commercial assays		
HQ Silver Enhancement Kit	Nanoprobes	Cat. # 2012
Experimental models: Organisms/strains		
Mouse: Shank3B KO	Jackson Laboratory	RRID: IMSR_JAX:017688
Software and algorithms		
ImageJ (Fiji) software	NIH	https://fiji.sc/
MATLAB	Mathworks	https://www.mathworks.com/products/matlab.html
MClust 4.4.07	Redish Lab	https://github.com/adredish/MClust-Spike-Sorting-Toolbox
Prism 9	GraphPad Software	https://www.graphpad.com/

RESOURCE AVAILABILITY

Lead contact

Further information and requests for resources and reagents should be directed to and will be fulfilled by the lead contact, Zhanyan Fu (zfu@broadinstitute.org).

Materials availability

This study did not generate new unique reagents.

Data and code availability

- All original data reported in this paper will be shared by the lead contact upon request.
- This paper does not report original code.
- Any additional information required to reanalyze the data reported in this paper is available from the lead contact upon request.

EXPERIMENTAL MODEL AND STUDY PARTICIPANT DETAILS

Animal studies

Male mice were used for all the experiments. All mice were bred onto a C57BL/6J background. Mice were housed in groups of 2–4 with a standard 12h light/dark cycle (lights on at 7 a.m., lights off at 7 p.m.). The food and water was available *ad libitum*. All behavioral

experiments were conducted during the light cycle except for long term sleep recordings. Littermates were randomly assigned to different groups prior to experiments. All experiments were done in accordance with NIH guidelines and approved by the Fourth Military Medical University, the Broad Institute and MIT Institutional Animal Care and Use Committee. Experimenters were blinded to genotypes and treatment conditions for data collection and analysis.

Retrospective case studies

The retrospective case series comprised patients diagnosed with ASD as the DSM-V criteria at the Xi'an Hospital of Encephalopathy between January 2013 and October 2022, and Second Xiangya Hospital between November 2018 and August 2023. Because of the anticonvulsant role of lamotrigine in clinical practice, all 40 patients (male and female Chinese patents aged between 2 and 14 years old) included in the retrospective study were with epilepsy. See Figure 7A for detailed information of the patients in three groups. All patients continued to receive standard supportive therapies such as applied behavior analysis therapy, speech therapy, TCM therapy during the treatment regimen. The including patients met the following criteria: (1) > 2 years and <14 years of age at the time of starting the treatment regimen; (2) treatment regimen was during hospitalization and more than 2 months; (3) CARS2-ST score >30; (4) only one anticonvulsant (lamotrigine or levetiracetam) or no anticonvulsant was used during the treatment regimen; (5) no other chronic medical condition; (6) no associated global developmental delay; (7) normal brain MRI; (8) complete evaluation information before and after the treatment regimen.

METHOD DETAILS

Immunohistochemistry

Immunohistochemistry experiments were performed following the procedures described previously. Briefly, the mice were deeply anesthetized with isoflurane and transcardially perfused with 50 mL 0.01M phosphate-buffered saline (PBS; pH 7.4) followed by 100 mL 4% paraformaldehyde (PFA) in phosphate buffer (pH 7.4). Brains were removed and postfixed with the same fixative for 4h at 4°C. Then the brains were transferred to a 30% PB-buffered sucrose solution for 72 h at 4°C for cryoprotection. Coronal sections (30 μm) were cut with a freezing microtome (CM1950, Leica). The sections were incubated overnight at room temperature with Rabbit anti HCN2 antibody (1:200; Alomone labs, APC-030). Sections were washed with PBS (3 × 5 min) and then incubated with 4 μg/mL Alexa Fluor 594-conjugated anti-mouse IgG (Invitrogen, A-11012) at room temperature for 4h. Sections were then washed in PBS (3 × 5 min) and incubated with DAPI (1:1000, Invitrogen, D1306) for 10 min. Sections were mounted onto slides and coverslipped with Fluoromount mounting media. Images were taken using a confocal microscope (FV3000, Olympus, Japan). ImageJ was used to manually measure the fluorescence intensity.

Pre-embedding immunogold-silver cytochemistry

Mice were deeply anesthetized with isoflurane and transcardially perfused with PBS (pH 7.4) followed by 50 mL of ice-cold mixture of 4% PFA and 0.05% glutaraldehyde in 0.1 M PB. The brains were removed and postfixed by immersion in the same fixative for 4h at 4°C. Serial coronal sections at 50 μm thicknesses were collected with a vibratome (VS1000s, Leica). Sections were blocked for 2h in PBS containing 5% bovine serum albumin (BSA), 5% normal goat serum (NGS) and 0.05% Triton X-100. Then the sections were incubated in the primary antibody of Rabbit anti HCN2 (1:800, Alomone labs, APC-030), diluted in PBS containing 1% BSA, 1% NGS and 0.05% Triton X-100 for 18 h at room temperature. After rinsing in PBS, the sections were transferred in anti-rabbit IgG conjugated to 1.4 nm gold particles (1:100, Nanoprobes). After that, the sections were rinsed and postfixed in 2% glutaraldehyde in PBS for 45 min. Signals of HCN2 immunoreactivity were detected by silver enhancement kit (HQ silver kit, Nanoprobes). Sections were rinsed with deionized water and then postfixed in 0.5% osmium tetroxide in 0.1 M PB for 2h. Then they were dehydrated with grade ethanol, replaced with propylene oxide, and embedded in Epon 812 between plastic sheets. After polymerization, the sections were selected under the light microscope, trimmed under a stereomicroscope, and glued onto blank resin stubs. Serial ultrathin sections were then cut with a diamond knife (Diatome, Hatfield) and an Ultramicrotome (EM UC6, Leica). The sections were mounted on formvar-coated mesh grids (6 sections/grid). After that, sections were counterstained with uranyl acetate and lead citrate for electron microscopic examination. We captured the images under the electron microscope (JEM-1230, JEOL LTD). The density and linear density were measured as previous described[73] with ImageJ software.

Viral vectors

AAV1-hSyn-CHETA-eYFP was produced by Addgene (Watertown, MA, USA). AAV1-hSyn-HCN2-*c*-Ha-Ras farnesylation signal-P2A-mcherry and AAV1-hSyn-*c*-Ha-Ras farnesylation signal-P2A-mcherry were constructed and produced by OBiO Technology (Shanghai, China). The viral titer was (2–5) $\times 10^{12}$ particles/mL. All viral vectors were aliquoted and stored at −80°C until used.

Stereotaxic surgery

Virus injections for optogenetics and patch clamp were administered to mice aged 2 months old. For HCN2 overexpression experiments, the mice received virus injection at P21. All surgeries were performed under aseptic conditions and the animals were maintained their body temperature with a heating pad. The mice were anesthetized with isoflurane (4% for induction and 1.5% for

maintenance), and their heads were fixed in a stereotaxic injection frame (RWD Life Science Inc.). All skull measurements were made relative to bregma.

For all virus injection, we used a glass micropipette containing 250 nL viral solution to reach the VPM (AP = −1.50 mm, ML = 1.75 mm, DV = 3.50 mm), PrV (AP = −4.90 mm, ML = 2.00 mm, DV = 4.50 mm), S1 (AP = −1.50 mm, ML = 3.00 mm, DV = 1.20 mm) or 100 nL RetroBeads IX to S1 (AP = −1.50 mm, ML = 3.00 mm, DV = 1.20 mm). We delivered the virus at a rate of 50 nL/min using a microsyringe pump (Kd Scientific). Following the viral injection, the micropipette was held at the site for 10 min to allow diffusion of the virus. Then the incision was closed with vetbond and mice recovered in a clean cage on a heating pad.

For multi-electrode array implantation, craniotomy was drilled centered at AP = −1.50 mm and ML = 1.75 mm for VPM recordings, at AP = −1.50 mm, ML = 3.00 mm for S1 field recordings. The dura was carefully removed and the drive implant was put into the target region with a stereotaxic arm. Surgilube was smeared around the electrodes to protect from dental cement. Stainless steel screws were put into the skull as the ground and EEG electrodes. An EMG electrode was put into the neck muscles. The whole construct was bonded together to the skull using dental cement (Parkell, Edgewood NY). For head-fixed recordings, we added a homemade 3D-printed hexagonal plastic crown to the base of micro-electrode array.

For EEG/EMG electrode implantation, we put an intracranial frontal EEG electrode screw at AP = 1.50 mm and ML = 1.50 mm, and an intracranial parietal EEG electrode screw at AP = −1.30 mm and ML = 2.30 mm to pick up the EEG signals with common ground/reference electrode screw above the cerebellum. The EMG electrodes were put into the nuchal muscle of mice. The electrodes were secured by dental cement and soldered to EEG/EMG headmount (Pinnacle Technology).

All the post-surgery mice were given injected analgesics (1 mg/kg sustained-release Buprenorphine as analgesic after the surgery) every 72h or as needed.

Western blot

Western blot was performed as described previously.[8] Briefly, the VPM tissues were collected after coronal dissection and sonicated in RIPA buffer (Sigma-Aldrich, R0278) containing a 1:100 ratio of protease and phosphatase inhibitor cocktail (Thermo Scientific, #1861284). The protein samples were quantified by bicinchoninic acid assay (Thermo Scientific, A53225), resolved in sodium dodecyl sulfate-polyacrylaminde gel electrophoresis (SDS-PAGE), and transferred to polyvinylidene difluoride membranes. Membranes were blocked with 5% nonfat dry milk in tris-buffered saline-tween 20 (TBST) for 2h at room temperature, and then incubated with primary antibodies at 4°C overnight. The following antibodies were used: Rabbit anti HCN1 (1:400, Alomone lab, APC-056), Rabbit anti HCN2 (1:500, Alomone lab, APC-030), Rabbit anti HCN4 (1:200, Alomone lab, APC-052), Rabbit anti Na-K-ATPase (1:1000, Cell signaling Technology, #3010), Mouse anti β-actin (1:1000, Cell signaling Technology, #3700). After primary antibody incubation, membranes were rinsed with TBST (3 × 10 min) and subsequently incubated with horseradish peroxidase conjugated-secondary antibodies. Proteins were visualized with the enhanced chemiluminescence detection method (Advansta). The scanned images were quantifies using ImageJ software. Specific bands were then quantified and normalized to β-actin loading control for each lane and each blot.

For the synaptoneurosomal protein measurement, we prepared the crude synnaptoneurosomal as previously described.[40] The VPM tissue was dissected and homogenized in a solution containing 0.32 M sucrose, 20 mM HEPES (pH 7.4), and protease inhibitor cocktail. The homogenate was centrifuged for 10 min at 2,800 rmp at 4°C. The supernatant was centrifuged at 14,000 rmp for 10 min and the pellet (crude synaptoneurosomal) was washed in homogenizing buffer. It was solubilized in protein lysis buffer for 10 min at room temperature. Then we performed western blot assay as above described.

Behavioral tests

For acute LTG treatment in adult mice, 8–12-week male *Shank3* KO and their littermate WT mice were randomly intraperitoneal injected with LTG (2% DMSO in saline) at 20 mg/kg or with vehicle. After treatment, the mice were put back to their home cages gently in the behavioral test room for habituation. After 30 min, we performed behavioral assessments.

For LTG treatment during developmental stages, P7, P14 or P21 *Shank3* KO and their littermate WT mice were randomly subcutaneously injected with 20 mg/kg LTG for 5days or 7days. The behavioral tests were carried out at 12-week age old.

Whisker guided exploration (WGE) test

The test apparatus is an octagonal maze (66 cm × 52 cm × 30 cm) as previously described.[14] Various geometric shapes were placed at regular intervals along the apparatus walls. To arouse locomotor activity, mice were allowed to explore in the open field for 10 min before the test day. The light intensity was set at 10 Lux and the temperature was set at 24 (±1)°C during habituation and throughout the testing periods. On test day, mice were adapted to the testing room for 30 min before the WGE test. The test mouse was then allowed to explore the octagonal maze for 10 min. Between two consecutive tests, 75% ethanol was used to eliminate animal odor. The next test started until the ethanol had completely evaporated. The movements of mice were recorded and analyzed using SMART v.3.0 software (Panlab). Data were collected in terms of the total distance and the percentage of time spent in smooth or textual areas of the apparatus.

Whisker Nuisance (WN) test

The experiments and habituation steps were performed simultaneously between 1 h after the onset of the light phase (8:00 a.m. to 6:00 p.m.) and 1 h before the dark phase. After each experiment for each mouse, we used paper towels and 75% ethanol to clean the

smell of the last experiment. Each mouse had its own experimental cage, and a handful of bedding of each mouse was introduced to this experimental cage a few days before the formal experiment in order to eliminate stress by the environment. Habituation phase should be performed for three days before experiment, during the habituation phase, and each mouse was introduced into the experimental cage with their own bedding for 30 min. On the experiment day, we repeated the habituation phase. A wooden stick was then introduced into the experiment and the mouse was not stimulated by the stick that was shaking above the mouse for 5 min, which referred as sham phase. After the sham, we continuously stimulated the whiskers for 5 min for 3 consecutive rounds with a 1-min-interval. The behavioral assessment is based on manual video scoring of single behaviors. Five different categories are scored as previously described[14,42]: freezing (fearful behavior), stance, hyperventilation (over-breathing), aggressiveness (aggressive response to stick presentation) and evasiveness on a 0–2 points qualitative scale (0, absent; 1, scarcely present during the observation period; 2, present for most of the observation period).

Sleep recordings and scoring

After one-week recovery from EEG/EMG surgeries, mice were put into the sleep recording chamber with their home cage beddings inside for 48 h habituation. For the dataset of Figures 1, 5 and S10, EEG/EMG signals were collected for 72 h from the onset of the light phase (7 a.m.; ZT0). For the dataset of Figure 6, the mice were injected with 20 mg/kg LTG following 2 h habituation. 30 min after injection, the EEG/EMG signals were recorded. The signals were amplified, digitized continuously with the sampling rate of 1 kHz. The EEG/EMG signals were acquired with Sirenia Acquisition software (Pinnacle Technology). Sleep scoring was performed semi-manually with Sleep Sign software (KISSEI COMTEC).

Slice electrophysiological recordings

Whole cell patch clamp recordings were performed as previous described.[32] Briefly, the mice were anesthetized with isoflurane and transcardially perfused with ice-cold carbogenated (95% O_2, 5% CO_2) cutting solution containing the following (in mM): 194 sucrose, 30 NaCl, 1.2 NaH_2PO_4, 0.2 $CaCl_2$, 2 $MgCl_2$, 26 $NaHCO_3$, 10 D-(+)-glucose, 0.1 L-ascorbic acid and 0.4 sodium pyruvate (pH 7.4, 295–300 $mOsml^{-1}$). Coronal slices (220-μm) containing VPM were prepared with a vibratome (VT1200S, Leica) and were incubated for 30 min in a holding chamber at 32°C in cutting solution. Then the slices were transferred to an artificial cerebral spinal fluid (ACSF) solution containing the following (in mM): 119 mM NaCl, 2.3 KCl, 1.0 NaH_2PO_4, 26 $NaHCO_3$, 11 D-(+)-glucose, 1.3 $MgSO_4$ and 2.5 $CaCl_2$ (pH 7.4, 295–300 $mOsml^{-1}$) to recover at least for 1 h at room temperature before recording.

The resistance of the patch pipettes (King Precision Glass, KG33) was ∼ 4–6 MΩ. For the recording of EPSCs, pipettes were filled with an internal solution containing (in mM): 120 $CsMeSO_3$, 5 NaCl, 10 TEA-Cl, 10 HEPES, 1.1 EGTA, 4 Lidocaine, 4 MgATP, 0.3 Na_3GTP. For the recording of IPSCs, pipettes were filled with an internal solution containing (in mM): 110 CsCl, 12 $CsMeSO_3$, 30 TEA-Cl, 10 HEPES, 0.5 EGTA, 10 Phosphocreatine, 4 MgATP, 0.3 Na_3GTP. For the recordings of intrinsic properties, excitatory postsynaptic potentials (EPSPs) and Ih currents, pipettes were filled with an internal solution containing (in mM): 120 K-gluconate, 2 $MgCl_2$, 10 HEPES, 1.1 EGTA, 5 MgATP, 0.4 Na_3GTP, 10 Phosphocreatine. The recordings were made with a microelectrode amplifier with bridge and voltage clamp modes of operation (700B, Molecular Devices) filtered at 5 kHz and sampled at 20 kHz with a Digidata 1500B. Clampex 10.7 was used for acquisition and analysis. RetroBeads labeled neurons were identified with a microscope equipped with GFP or RFP filter (Olympus, BX-51WI).

To record the intrinsic properties, we measured the resting membrane potential (RMP) after break-in. The cells were held at different holding potentials (Vh = −50mV, RMP, −75 mV). Spikes were induced by incrementally increasing the current injection in current-clamp mode. Miniature excitatory postsynaptic currents (mEPSCs) and miniature inhibitory postsynaptic currents (mIPSCs) were recorded at Vh = −70 mV mEPSCs were recorded in the presence of 10 μM bicuculline, 50 μM APV and 1 μM tetrodotoxin. mIPSCs were recorded in the presence of 20 μM DNQX, 50 μM APV and 1 μM tetrodotoxin. To evoke AMPA receptor-mediated EPSPs, we followed a previously described protocol.[74] 40 Hz or 20 Hz of 2 ms duration optical stimulation was delivered in the current clamp mode. Each recordings contained 10 sweeps with 20s internals. Summation ratio was calculated with the 5^{th} peak of EPSP divided by 1^{st} peak of EPSP. To record the T-type Ca^{2+} channel-mediated current, we followed the protocol we reported previously.[15] We applied different hyperpolarizing steps (500 m, ranging from −110 to −60 mV) and recorded the current in voltage clamp configuration while applying the small conductance calcium-dependent potassium currents (SK) channel blocker apamin (100 nM).

In vivo electrophysiological recordings

After recovery from the multi-electrode assay implantation surgeries, mice were connected to 64-channel preamplifier headstage (Blackrock Microsystems) and the signals were amplified, filtered between 0.3 Hz and 7.5 kHz and digitized at approximately 30 kHz as previously described.[15] The LFP and EEG traces were amplified and filtered between 0.3 Hz and 250 Hz. Spikes were obtained through a high-pass filtering (250 Hz −7.5 kHz) and spike detection. We used the MClust toolbox (Redish Lab) to manually cluster the spikes, based on the amplitude and energy on the four electrodes of each tetrode. Units were separated by hand, and cross-correlation and autocorrelation analyses were used to confirm unit separation.

We classified the behavioral epochs into different states (Wake, REM, Non-REM) as above stated using simultaneously recorded EEG and EMG. We used the Sirenia sleep Pro v2.0.4 (Pinnacle Technology) to analyze sleep scoring in 10 s epochs.

Spikes and LFPs data were imported into MATLAB for analysis using custom-written functions. The bursts were identified as previous described.[75] At least two spikes with an inter-spike interval of less than 4 ms with the first spike in the burst preceded by silence

of at least 100 ms. The burst ratio was then computed through the number of burst spikes divided by the total number of spikes.[75] Only units for which >100 spikes were collected were considered for this study. During Wake, REM and Non-REM states, we computed the firing rate of individual VPM units with 0.1 s bin size, overlap 7/8 and computed the mean of all instantaneous binned firing rates as a measure of arousal-related modulation of VPM unit firing rate.

For sleep related analysis, the S1-LFP delta wave was obtained by filtering the S1-LFP signal in the 1–4 Hz frequency band via an order 3 butterworth forward-backward filter. The angle of the instantaneous phase (derived from a Hilbert transformation of the filtered S1-LFP) was computed by MATLAB function 'hilbert'. For each VPM unit, we constructed a spike-phase histogram (24 bins within 0–360; MATLAB function ''rose''). Units were considered significantly phase-locked when the distributions of spike phases significantly differed from a uniform distribution on the basis of Rayleigh's test for circular uniformity (cut-off, $p < 0.05$). To quantify the degree of phase-locking, the Pearson's correlation coefficient between spike counts and phase angle was computed for each unit. The phase locking strength was calculated from R-squared value of cosine fit as we previously described.[15] Analysis of the circular uniformity was performed in MATLAB using the circular statistics toolbox.

For whisker stimulation paradigm, the recordings were conducted in head-fixed mice trained to walk on a rotating running wheel. After the recovery from the surgery, the mice were trained to walk on the uniformly rotated wheel (controlled with National Instruments DAQ boards) for three 10-min sessions daily for one week. While recordings, the whiskers were restrained by placing them in a hoop made from silk suture thread that was closed 2–3 mm from the base of the whisker as previously described. The restrainer was attached to a piezo-electric plate bender (Noliac). The stimulus was a cosine wave onset with a time to peak of 6 ms (from caudal to rostral). The stimulation amplitudes and vibrissae deflections were calibrated using a high-speed camera. We delivered 0.3 mm and 1.0 mm deflection randomly with MATLAB-controlled stimulator with the interval of 12 s.

Patients and data collection

This study was performed according to the Declaration of Helsinki (1964) and approved by the Xi'an TCM Hospital of Encephalopathy Ethics Committee: Approval No. XNLL2022-09, Medical Ethics Committee of the Second Xiangya Hospital of Central South University: Approval No. 2018LSK-035.

After privacy processing, pairs of authors independently screened all case records and extracted the following data: gender, age at treatment initiation, season at treatment initiation, comorbidity, information of somatoscopy, medications and doses used, adverse effects, initial CARS2-ST and ABC score, the CARS2-ST and ABC score before medication starting, the CARS2-ST and ABC score at discharge (the end of observation period). A senior author checked for data integrity, accuracy, and consistency. Any disagreements were resolved through consensus or by recourse to a third author.

Stata 17.0 software and statistical program R 4.0.2 were used to calculate effects summary estimates. We defined the no AED intervention as the control group, LTG or LEV treatment was the treatment group. We first calculated the absolute change in CARS2-ST or ABC score, which was the end of observation score minus the baseline score. Either the CARS2-ST or ABC absolute change score were continuous outcomes with consistent measurement, weighted mean differences (WMD) and 95% CIs were used to evaluate the improvement effect comparing with the control group. To determine the factors contributing to the results, we conducted a multiple linear regression analysis to investigate the factors influencing the absolute changes of the ABC or CARS2-ST score. The dependent variable was the absolute changes of the ABC or CARS2-ST score, and the independent variables included gender, age, season of treatment, duration of observation regimen, body temperature, blood pressure, resting heart rate, body weight, basic score of CARS2-ST, basic score of ABC, and treatment.

QUANTIFICATION AND STATISTICAL ANALYSIS

Prism 9.0 (GraphPad Software) and SPSS 21.0 were used for statistical analysis of data. No statistical methods were used to predetermine sample sizes. Data were presented as means ± SEM, unless otherwise stated in the figure legends. The normality test was performed by the Shapiro-Wilk test. The homogeneity of variance test was tested using Levene's test. Normally distributed data with equal variance were tested using t tests (one-tail or two-tail, unpaired or paired), one-way ANOVA and repeated-measures ANOVA followed by Tukey's multiple comparison test. Datasets that were not normally distributed were analyzed with nonparametric tests. Details of particular statistical analysis can be found in Data S1. The use of asterisks indicates statistical significance ($^{*}p < 0.05$, $^{**}p < 0.01$, $^{***}p < 0.001$, $^{****}p < 0.0001$)